J. Fluid Mech. (2024), *vol*. 981, A20, doi:10.1017/jfm.2024.85

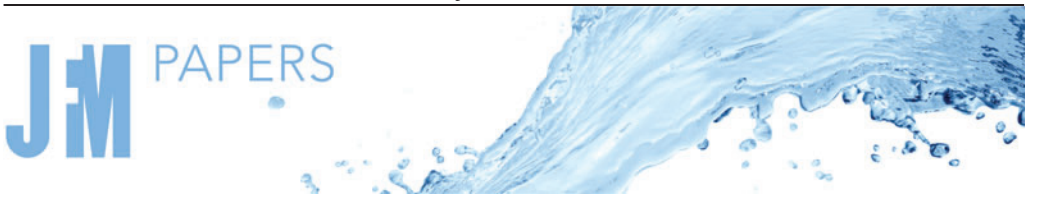

Robust relation of streamwise velocity autocorrelation in atmospheric surface layers based on an autoregressive moving average model

Fei-Chi Zhang[1], **Jin-Han Xie**[1,2,†], **Song Xi Chen**[3,†] **and Xiaojing Zheng**[1,4,†]

[1]Department of Mechanics and Engineering Science at College of Engineering, and State Key Laboratory for Turbulence and Complex Systems, Peking University, Beijing 100871, PR China

[2]Joint Laboratory of Marine Hydrodynamics and Ocean Engineering, Laoshan Laboratory, Shandong 266237, PR China

[3]School of Mathematical Sciences, Guanghua School of Management and Center for Statistical Science, Peking University, Beijing 100871, PR China

[4]Center for Particle-Laden Turbulence, Lanzhou University, Lanzhou 730000, PR China

(Received 7 July 2023; revised 18 January 2024; accepted 18 January 2024)

We construct an autoregressive moving average (ARMA) model consisting of the history and random effects for the streamwise velocity fluctuation in boundary-layer turbulence. The distance to the wall and the boundary-layer thickness determine the time step and the order of the ARMA model, respectively. Based on the autocorrelation's analytical expression of the ARMA model, we obtain a global analytical expression for the second-order structure function, which asymptotically captures the inertial, dynamic and large-scale ranges. Specifically, the exponential autocorrelation of the ARMA model arises from the autoregressive coefficients and is modified to logarithmic behaviour by the moving-average coefficients. The asymptotic expressions enable us to determine model coefficients by existing parameters, such as the Kolmogorov and the Townsend–Perry constants. A consequent double-log expression for the characteristic length scale is derived and is justified by direct numerical simulation data with $Re_\tau \approx 5200$ and field-measured neutral atmospheric surface layer data with $Re_\tau \sim O(10^6)$ from the Qingtu Lake Observation Array site. This relation is robust because it applies to Re_τ from $O(10^4)$ to $O(10^6)$, and even when the statistics of natural ASL deviate from those of canonical boundary-layer turbulence, e.g. in the case of imbalance in energy production and dissipation, and when the Townsend–Perry constant deviates from traditional values.

Key words: atmospheric flows, turbulent boundary layers

† Email addresses for correspondence: jinhanxie@pku.edu.cn, csx@gsm.pku.edu.cn, xjzheng@lzu.edu.cn

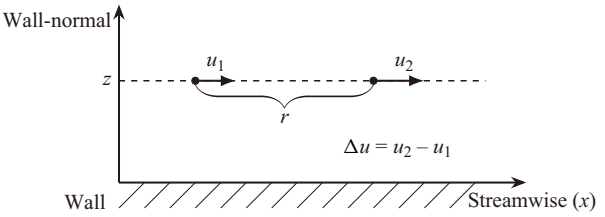

Figure 1. A schematic diagram of the two points in space used for autocorrelation and second-order structure function.

1. Introduction

Coherent structures are important for understanding boundary-layer turbulence (Robinson 1991; Schoppa & Hussain 2002; Jiménez 2018). In the logarithmic region, where the mean streamwise velocity logarithmically depends on the distance to the wall, z, and beyond, various types of coherent motions on a wide range of scales are important for flow dynamics, such as the wall-bounded eddies (Yang, Willis & Hwang 2019; Puccioni *et al.* 2023) and large-scale motions with a streamwise scale of the order of the boundary-layer thickness δ (Kim & Adrian 1999; Ganapathisubramani *et al.* 2005; Hutchins & Marusic 2007; Hutchins *et al.* 2012; Sillero, Jiménez & Moser 2014). These energy-containing motions contribute to the turbulent skin-friction generation (de Giovanetti, Hwang & Choi 2016), and transport of kinetic energy and Reynolds stress (Guala, Hommema & Adrian 2006; Balakumar & Adrian 2007; Wang & Zheng 2016). The two-point correlation of the fluctuating velocity (Wallace 2014) is widely used to identify the characteristic scales of these coherent structures (Kovasznay, Kibens & Blackwelder 1970; Tutkun *et al.* 2009; Bailey & Smits 2010; Liu, Wang & Zheng 2019*b*). The common practice is obtaining a length scale corresponding to an artificial correlation threshold (Zhou *et al.* 1999; Hutchins, Hambleton & Marusic 2005; Dennis & Nickels 2011). Liu, Wang & Zheng (2017) summarized the dependence of streamwise, spanwise and wall-normal characteristic length scales on the distance to the wall for varying friction Reynolds number Re_τ in a range of three orders of magnitude. In particular, using a threshold value of 0.05, the streamwise length scales normalized by δ show an approximate logarithmic dependence on z/δ. However, this intriguing dependence is empirical and remains to be understood.

We focus on the two-point correlation of streamwise velocities, i.e. the autocorrelation, with a fixed distance to the wall, illustrated in figure 1. The autocorrelation R_{uu} relates to the second-order structure function through

$$\langle \Delta u^2(r) \rangle = \langle [u(\boldsymbol{x}_1 + r\boldsymbol{e}_{\boldsymbol{x}}) - u(\boldsymbol{x}_1)]^2 \rangle = 2\langle u^2 \rangle - 2\langle u_1 u_2 \rangle = 2\langle u^2 \rangle - 2R_{uu}(r), \tag{1.1}$$

where $u_1 = u(\boldsymbol{x}_1)$ and $u_2 = u(\boldsymbol{x}_1 + r\boldsymbol{e}_{\boldsymbol{x}})$, with $\boldsymbol{e}_{\boldsymbol{x}}$ the unit vector in the streamwise direction, are fluctuating velocities at two points with streamwise displacement r, and the angular brackets denote the ensemble average. Thus, we can understand the behaviour of autocorrelation based on the existing theories of the second-order structure function $\langle \Delta u^2 \rangle$.

Different ranges of the second-order structure function are discovered in the logarithmic region. In the dissipation range, where r is of or smaller than the order of the Kolmogorov microscale $l_\nu = (\nu^3/\epsilon)^{1/4}$ with ν the viscosity and ϵ the energy dissipation rate, $\langle \Delta u^2 \rangle \sim r^2$ (Frisch 1995). For scales larger than l_ν, three ranges depicted in figure 2 are defined (cf. Chamecki *et al.* 2017). The inertial range covers the scales between the dissipation scale (l_ν) and the distance to the wall (z), where Kolmogorov's expression

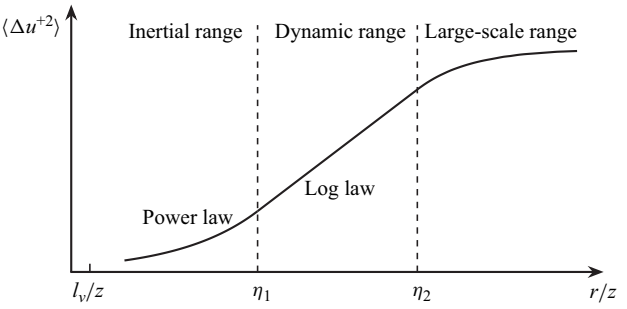

Figure 2. An illustration of the three ranges of the second-order structure function in log-normal coordinates. Here, η_1 and η_2 are the dimensionless lower and upper ends of the dynamic range.

(Kolmogorov 1941) well describes the second-order structure function (de Silva *et al.* 2015). With intermittency considered, Anselmet *et al.* (1984) proposed to express $\langle \Delta u^2 \rangle$ as

$$\langle \Delta u^2 \rangle = C_2 (\epsilon r)^{2/3} \left(\frac{r}{l} \right)^{\xi_2 - 2/3}, \tag{1.2}$$

where C_2 is the Kolmogorov constant, l is a characteristic length scale and the departure of ξ_2 from $2/3$ captures the turbulent intermittency (Meneveau & Sreenivasan 1987; She & Leveque 1994). de Silva *et al.* (2015) chose $l = z$, and by introducing the local production-dissipation balance $\epsilon \approx u_\tau^3/(\kappa z)$ (Pope 2000) with u_τ the friction velocity and κ the von Kármán constant, they obtain

$$\langle \Delta u^{+2} \rangle = M_2^* \left(\frac{r}{z} \right)^{\xi_2}, \quad l_\nu \ll r < z, \tag{1.3}$$

where the superscript '+' denotes the velocity increment normalized by u_τ and $M_2^* = C_2 \kappa^{-2/3}$. For scales larger than z but smaller than the boundary layer thickness δ, the dynamic range, the shear-dominant flow leads to significant anisotropy and $\langle \Delta u^{+2} \rangle$ shows a logarithmic dependence on r, i.e. (Davidson, Nickels & Krogstad 2006*b*)

$$\langle \Delta u^{+2} \rangle = A_2^* + B_2^* \ln \left(\frac{r}{z} \right), \quad z < r \lesssim \delta, \tag{1.4}$$

where A_2^* and B_2^* are constants. The shear production term $-\langle \Delta u \Delta w \rangle \, \mathrm{d}U/\mathrm{d}z$ leads to the logarithmic expression over the scale range from z to δ (Pan & Chamecki 2016; Xie *et al.* 2021). In this range, the pressure-strain-rate correlation is important in the energy redistribution between different velocity components (Ding *et al.* 2018). Additionally, from the perspective of inactive eddies that contribute to streamwise velocity fluctuations but not to the shear stress (Townsend 1961; Marusic & Kunkel 2003; Ding *et al.* 2018), this range can also be called the 'inactive range'.

Assuming that there is no distinguished range between inertial and dynamic ranges, Xie *et al.* (2021) matched the above two ranges at $r = z$ and determined $A_2^* = M_2^*$ and $B_2^* = M_2^* \xi_2$. In the above analysis, u_τ captures the characteristic velocity and the characteristic length scale l is chosen to be z. In contrast, Davidson & Krogstad (2014) studied boundary-layer turbulence without local production–dissipation balance and proposed a characteristic length scale $l_\epsilon = u_\tau^3/\varepsilon$. Pan & Chamecki (2016) extended the use of l_ε as a characteristic scale to the vegetation canopy where a significant imbalance between

local production and dissipation exists. Moreover, Chamecki *et al.* (2017) investigated the l_ε-dependence in the dynamic range for neutral and stable atmospheric surface layers (ASLs), and obtained the 2/3-power expression for convective ASL turbulence, which is consistent with the $-5/3$ law of spectra predicted by Kader & Yaglom (1989) and Yaglom (1994) in the freely convective atmospheric boundary layer and first interpreted by Tong & Nguyen (2015) in convective ASL.

The power and logarithmic expressions in the inertial and dynamic ranges are also obtained for the third-order structure function (Xie *et al.* 2021). Using ASL data measured at the Qingtu Lake Observation Array (QLOA) site, in Minqin District, Gansu Province, PR China, Zhang, Xie & Zheng (2022) compared the choice of $l = z$ and $l_\varepsilon = u_\tau^3/\varepsilon$, and argued that z is also suitable for ASL turbulence with unbalanced energy production and dissipation rate if u_τ is replaced by $(\varepsilon z)^{1/3}$ as the characteristic velocity scale. In the present work, we do not aim to distinguish the appropriate normalization scale. Following the range division by Chamecki *et al.* (2017) (cf. figure 2), we choose u_τ as the characteristic velocity and z as the characteristic spatial scale for structure functions. For convective ASL, the buoyancy effects hold significant importance. This gives rise to another scale range characterized by the $-5/3$ law of spectra (Tong & Nguyen 2015; Tong & Ding 2019) and 2/3 power law of second-order structure function (Chamecki *et al.* 2017). We refer to the scales beyond the dynamic range as the large-scale range. Large- and very-large-scale motions that exist in this range have been extensively studied in terms of their contribution to turbulent kinetic energy and Reynolds stress (Balakumar & Adrian 2007; Lee & Sung 2011; Wang & Zheng 2016). However, the autocorrelation in this range lacks a thorough investigation and is one of the main subjects of the present study.

Several simplified models were proposed since many empirical statistical results have been discovered in boundary-layer turbulence. A notable instance is Townsend's attached eddy model (AEM) (Townsend 1976). In the logarithmic region, the characteristic eddies are assumed to be geometrically self-similar with kinetic energy scales as u_τ^2. AEM well captures velocity statistics, such as the logarithmic dependence of the second-order structure function (cf. (1.4)) (Davidson & Krogstad 2014; Yang *et al.* 2017; Xie *et al.* 2021), and it can also describe higher-order statistics after refinement (Marusic & Monty 2019). In this work, we combine turbulence knowledge, particularly the characteristic scales and the logarithmic expression of structure functions, and time-series statistical methods to explore the global behaviour, which covers the three inviscid ranges, of the second-order structure function.

Several statistical methods have been used to analyse turbulence data obtained in experiments or field measurements as time series, and to perform digital simulation (Di Paola 1998; Krenk & Møller 2019) and forecast of wind field velocity (Sfetsos 2002; Kusiak, Zheng & Song 2009). Stationary time series can be analysed using the spectral and sequential methods (Kleinhans *et al.* 2009; Schmitt & Huang 2016; Schmidt *et al.* 2018), and often these two are combined. Here we adopt the sequential method because the spectral method is more computationally demanding (Kareem 2008) and because the sequential method yields results directly linked to measured data.

Specifically, we apply an autoregressive moving average (ARMA) model (Shumway, Stoffer & Stoffer 2000), which has broad applicability in engineering applications and theoretical studies of turbulence, particularly in complicated situations where unknown or unresolved impacts may exist. The autoregressive (AR) part of ARMA model assumes that the variable at the current moment is affected by past moments, and the moving average (MA) part models the other unknown effects with a series of noises. For instance, the

Langevin equation, which is identical to the first-order AR model, was used to describe the Lagrangian velocities in the inertial range (Thomson 1987). The application of AR and ARMA models for wind field simulation is described by Rossi, Lazzari & Vitaliani (2004). In addition, the ARMA model can detect and replace the spikes or outliers in turbulent velocity data due to Doppler noise and signal aliasing (Razaz & Kawanisi 2011; Dilling & MacVicar 2017). Faranda *et al.* (2014*a*,*b*) tested the applicability of the ARMA model in a turbulent von Kármán swirling flow and remarked that the ARMA model is effective in discriminating different flows. Without prior knowledge, events with undetermined physical mechanisms can be extracted from time series by distinguishing them from the white noise and/or first-order AR process, which, after classification, contributes to the understanding of stable ASL turbulence (Kang, Belušić & Smith-Miles 2014, 2015). Extended AR models for multivariate situations combined with data clustering methods were used to investigate interactions between motions with distinct characteristic scales (Vercauteren & Klein 2015; Vercauteren, Mahrt & Klein 2016; Vercauteren *et al.* 2019). Moreover, the ARMA model and its combination with other statistical models can be used to analyse and predict non-stationary ASL turbulence (Zhang *et al.* 2023).

Our goal is to apply the stochastic equation of the ARMA model to the streamwise velocity series to capture the behaviours of dynamic and large-scale ranges in the logarithmic region of boundary-layer turbulence. Specifically, we aim: (i) to provide a procedure for applying the ARMA model to boundary-layer turbulence; (ii) to provide explanations of parameters in the ARMA model; (iii) to extend the existing theoretical expressions for the second-order structure function to the large-scale range using the analytical expressions based on the ARMA model; and (iv) to explain the behaviour of streamwise characteristic length scales in the logarithmic region and propose an analytical expression that explains experimental and measured data. The ASL data measured from QLOA with high friction Reynolds number ($Re_\tau \sim O(10^6)$), which could deviate from the typical states of canonical boundary-layer turbulence due to complicated environmental impacts, is used as an example to justify and show the robustness of the obtained expressions.

The rest of this paper is organized as follows. In § 2, we introduce the ARMA model and construct the ARMA model in boundary-layer turbulence. The model application procedure and the analytical expressions are also presented. We present the details of ASL data and perform data analysis and theory verification in § 3. The main results are summarized and discussed in § 4. Appendix A contains the basic properties and details about the ARMA model, and an approximate derivation of the ARMA model parameters leading to the logarithmic expression in the dynamic range is shown in Appendix B. The uncertainty in determining the global expression is discussed in Appendix C.

2. The ARMA model

Although different velocity components are nonlinearly coupled in the Navier–Stokes equation, for model simplicity, we assume the streamwise velocity to be autocorrelated to permit a one-dimensional model. In the context of this paper, 'autocorrelation' refers to the correlation function of streamwise velocity evaluated at different times or locations, and we fix the distance to the wall z located in the logarithmic region. Under these assumptions, we can apply the ARMA model to stationary streamwise velocity time series in boundary-layer turbulence.

For a stationary fluctuating velocity series $\{u_t\}$, the ARMA(p, q) model is

$$u_t = \sum_{i=1}^{p} \alpha_i u_{t-i\Delta t} + \sum_{j=1}^{q} \beta_j \epsilon_{t-j\Delta t} + \epsilon_t, \tag{2.1}$$

where p and q are the model orders, α_i with $i = 1, \ldots, p$ and β_j with $j = 1, \ldots, q$ are the model parameters, $\epsilon_{t-i\Delta t}$ with $i = 0, 1, \ldots, q$ are independent and identically distributed white noise with variance σ_ϵ^2, Δt is the time step, and the subscript t indicates the evaluation time t. The maximum model order is referred to as the model's memory depth, which indicates the maximum time range of the current moment to be directly affected. The model applicability and stationarity impose constraints on the model parameters, which are shown with details in Appendix A.

When applying the ARMA model, the orders p and q and the time step Δt should be determined first. In the traditional application of the ARMA model for time series analysis, the corresponding orders are generally empirically determined from the data without known basis (Shumway *et al.* 2000). If the orders are too small, the data cannot be well fitted; if the orders are too large, more computational effort is needed, which may lead to overfitting. In addition, if the autocorrelation of the data extends over a long time, directly adopting the raw data series with a time step of Δt_0, which corresponds to the measurement frequency, will result in an excessive number of model orders. In this case, a new time series with a time step $\Delta t > \Delta t_0$ should be resampled from the original series at equal intervals. Overall, there exist uncertainties in the choice of both order and time step of the ARMA model, which requires careful deliberation.

For boundary-layer turbulence, (1.3) and (1.4) present the expressions of streamwise-velocity autocorrelation in the inertial and dynamic ranges, but in the large-scale range, the behaviour of autocorrelation remains obscure. Since the ARMA model provides a global analytical expression for autocorrelation, we attempt to extend the second-order structure-function expression to the large-scale range by modelling the dynamic range with the ARMA model. We focus on the dynamic-range modelling for the following reasons. Since the dominant balances are distinctive in the inertial and dynamic ranges, an ARMA model with a fixed order is not applicable simultaneously in these two regimes. In addition, the large scale separation between the inertial and the dynamic range leads to excessive memory depth of the ARMA model. Therefore, we limit the minimum and maximum time ranges, which correspond to the model orders and the dynamic range of the second-order structure function, respectively. Thus, the autocorrelation has an asymptotically exponential decay in the large-scale range following the ARMA model (see Appendix A, (A13)).

2.1. *Constructing the ARMA model in boundary-layer turbulence*

The ARMA model applies to a time series, which links to a spatial second-order structure function under Taylor's frozen hypothesis (Taylor 1938). For a measured streamwise turbulent velocity time series with a time step Δt_0, mean streamwise velocity U and wall-normal position z, we extract a coarse series that does not resolve the small-scale inertial range. So the time step Δt of the extracted series satisfies

$$U\Delta t \approx \eta_1 z, \tag{2.2}$$

where η_1 corresponds to the scale that separates the inertial and dynamic ranges. The new series can be obtained by extracting one point for every $\Delta t/\Delta t_0$ points from the original series.

The larger scale η_2 bounds the memory depth of the model, i.e.

$$U\Delta t \max\{p, q\} \approx \eta_1 z \max\{p, q\} \approx \eta_2 z, \tag{2.3}$$

where p and q are undetermined, but at least one of them should equal η_2/η_1. Then in the large-scale range, the autocorrelation (cf. (A13)) takes the form

$$R_{uu}(r) = \sum_{i=1}^{p} c_i \exp\left(\frac{r}{\Delta x}\ln\lambda_i\right), \quad r \geq \eta_2 z, \tag{2.4}$$

with the corresponding second-order structure function

$$\langle \Delta u^2 \rangle = 2\langle u^2 \rangle - 2\sum_{i=1}^{p} c_i \exp\left(\frac{r}{\Delta x}\ln\lambda_i\right), \quad r \geq \eta_2 z, \tag{2.5}$$

where a set of exponential functions approximate the large-scale behaviour of $\langle \Delta u^2 \rangle$, and c_i and λ_i with $i = 1, \ldots, p$ are constants related to the model parameters (cf. (A13) and (A14)). In (2.5), a higher order p means the more likely it is to better approximate $\langle \Delta u^2 \rangle$. However, the parameters c_i need to be determined by the autocorrelation of the data, and the roots x_i need to be determined by the model parameters through the fitting procedure. We take a first-order approximation to obtain a more intuitive expression, i.e. $p = 1$, then (2.3) leads to $q = \eta_2/\eta_1$. Additionally, the model equation (cf. (2.1)) is reduced to

$$u_t = \alpha u_{t-\Delta t} + \epsilon_t + \sum_{j=1}^{q} \beta_j \epsilon_{t-j\Delta t}. \tag{2.6}$$

Here, the velocity u at the time t depends on the value of u at the previous time $t - \Delta t$ and is subject to random effects with memory depth q. The properties of autocorrelation of the ARMA model are presented in Appendix A.

When the two-point displacement is beyond the dynamic range, i.e. $k > q$, the autocorrelation becomes (cf. (A13))

$$R_{uu}(k\Delta x) = \alpha R_{uu}((k-1)\Delta x) = \alpha^{k-q} R_{uu}(q\Delta x) = \frac{R_{uu}(q\Delta x)}{\alpha^q}\exp(k\ln\alpha). \tag{2.7}$$

Replacing $k\Delta x$ with r, (2.7) becomes

$$R_{uu}(r) = \frac{R_{uu}(\eta_2 z)}{\alpha^q}\exp\left(\frac{\ln\alpha}{\Delta x}r\right), \quad r > \eta_2 z. \tag{2.8}$$

Thus, the autocorrelation implies an exponential decay in the large-scale range since $\alpha < 1$, which is similar to the approximation for correlations in homogeneous turbulence (Taylor 1921; Tennekes 1979, 1982).

The AR part of the ARMA model is regarded as the memory effect of flow and mainly controls large-scale motions, and the MA part does not contribute to the large-scale autocorrelation directly. If there is no MA part, the autocorrelation of the ARMA model decays exponentially as the displacement increases. In the dynamic range, the MA part contributes to the autocorrelation (cf. (A9)) and with a further constraint that the MA coefficients follows a power expression with exponent -2, the autocorrelation has a logarithmic dependence on the displacement, which is discussed in Appendix B.

2.2. *Linking between ARMA and AEM*

Based on the analytical expression of the ARMA model, similar to the AEM, the linear additive form of the MA part in the ARMA model leads to the logarithmic expression. AEM interprets the logarithmic expression of the dynamic range of second-order structure function based on the streamwise velocity representation (Yang *et al.* 2017)

$$u = \sum_{i=1}^{N_z} a_i, \tag{2.9}$$

where a_i is the random velocity increment induced by the attached eddies of size $\delta/2^i$ and N_z is the number of attached eddies contributing to u. Namely, the fluctuating velocity u is generated by random eddies with vertical sizes ranging from z to δ, and other potential effects are neglected. Noteworthily, the ARMA model equation (2.1) also contains random variables and the velocity memory. Similar to AEM, we interpret the MA part of the ARMA model as the random effect arising from turbulent eddies. The MA coefficients can be seen as the eddy population density and the random increment ϵ has the same strength. The above analysis is consistent with the interpretation of the ARMA model by Faranda *et al.* (2014*b*) that the AR part is linked to the contribution of the large scales and the MA part corresponds to the effects of eddies and correlation structure. This physical picture also guides us to characterize the dynamic range, from which the model orders are determined.

As mentioned before, the model orders are determined according to the scale information of boundary layers. By Taylor's frozen hypothesis, we can obtain $\Delta x = U\Delta t$ (cf. (2.2)) and in the ARMA$(1, q)$ model, Δx is considered as the minimum attached eddy's size, which is of $O(z)$. The memory depth of the model corresponds to the maximum attached eddy's size, $q\Delta x \approx \eta_2 z$, which is of $O(\delta)$ and represents the largest scale of the dynamic range. These scales are also important in AEM. Therefore, the ARMA model can be regarded as a stochastic form of AEM: a set of random white noise, whose scale range is consistent with the sizes of attached eddies, drives the fluctuating velocity. Additionally, in the ARMA model, the MA coefficients β_i with i from 1 to q quantify the distribution of attached eddies' effects (see Appendix B). As shown in figure 8(b) (§ 3.2), the -2 exponent in the power function of MA coefficients is consistent with the eddy population density in some AEM studies (de Silva, Hutchins & Marusic 2016; Hu, Dong & Vinuesa 2023). In addition, since the model's stationarity requires $\alpha < 1$, the lag term in (2.6) damps this linear dynamical system energized by random noise. Unlike the linear additive process model (cf. (2.9)) proposed for AEM, the ARMA$(1, q)$ model hypothetically presents a simple stochastic model of AEM, from which the long-term behaviour of the autocorrelation can be explored. Though Davidson & Krogstad (2009) provided a general expression for autocorrelation resulting from the attached eddies' contribution, eddy shape needs to be assumed, and they did not discuss the expression's large-scale behaviour. One advantage of the ARMA model is that the large-scale autocorrelation is obtained without assuming the eddy shape due to the capturing of the memory effect.

2.3. *Asymptotic expression of second-order structure function*

Even though the ARMA model provides an analytical expression for the second-order structure function in the dynamic and large-scale ranges, this complicated expression is not practically convenient. So in this section, we obtain a global expression covering the inertial, dynamic and large-scale ranges of the second-order structure function by

asymptotic matching. As aforementioned, the second-order structure function follows a logarithmic expression in the dynamic range (cf. (1.4)). More generally, in shear flows where the ratio of energy production rate to dissipation rate P/ε varies with wall-normal location z, which is not rare in ASL turbulence, the two ranges also match at an intermediate scale influenced by P/ε (Zhang *et al.* 2022). For the general case, (1.2) becomes

$$\langle \Delta u^{+2} \rangle = \frac{C_2}{(\kappa P/\varepsilon)^{2/3}} \left(\frac{r}{z}\right)^{\xi_2} = M_2 \left(\frac{r}{z}\right)^{\xi_2}, \quad l_\nu \ll r < z, \tag{2.10}$$

where M_2 may be a height-dependent constant due to the presence of P/ε. Assuming that the dimensionless lower and upper ends of the dynamic range are $r/z = \eta_1$ and $r/z = \eta_2$, respectively, we can perform the Taylor expansion on (2.10) and (1.4), and obtain the general form of (1.4) by matching at $r/z = \eta_1$:

$$\langle \Delta u^{+2} \rangle = A_2 + B_2 \ln\left(\frac{r}{z\eta_1}\right), \quad \eta_1 < \frac{r}{z} < \eta_2, \tag{2.11}$$

where

$$A_2 = M_2 \eta_1^{\xi_2}, \quad B_2 = M_2 \eta_1^{\xi_2} \xi_2, \tag{2.12a,b}$$

and they are obtained by matching (1.3) and (2.11) at η_1. The matching process links the dynamic-range coefficients A_2 and B_2 with the inertial-range coefficients M_2 and ξ_2, reducing two free parameters. The empirical value of η_1 is $O(1)$ (Davidson, Krogstad & Nickels 2006*a*; Davidson & Krogstad 2009; de Silva *et al.* 2015; Xie *et al.* 2021), corresponding to a length scale of $O(z)$. For the canonical case, by setting $C_2 = 2, \kappa = 0.4$, $\xi_2 = 2/3$ and $\eta_1 = 1$, we calculate from (2.12*a*,*b*) to obtain $A_2 \approx 3.68$ and $B_2 \approx 2.46$, whose values are close to previous research (Meneveau & Marusic 2013; de Silva *et al.* 2015; Xie *et al.* 2021).

In § 2.2, the ARMA model is analogous to a stochastic AEM and the attached eddies are modelled as a set of random effects. The logarithmic dependence of $\langle \Delta u^{+2} \rangle$ can also be obtained from the ARMA model under the assumption of self-similarity with $\beta_i \sim i^{-2}$. The details can be found in Appendix B.

In the large-scale range with scales larger than $\eta_2 z$, conventional AEM does not provide information on the structure functions. The advantage of the ARMA$(1, q)$ model is that it naturally provides an exponential autocorrelation for large scales (cf. (2.8)), i.e.

$$\langle \Delta u^{+2} \rangle = 2\langle u^{+2} \rangle - D_2 \exp\left(-E_2 \frac{r}{z}\right), \quad \frac{r}{z} > \eta_2, \tag{2.13}$$

where D_2 and E_2 are positive constants. Assuming that there is no distinguished range between the dynamic and the large-scale ranges, we match the expression in these ranges to determine three unknown parameters η_2, D_2 and E_2. By defining $r' = r/z$, we expand (2.11) and (2.13) to

$$\langle \Delta u^{+2} \rangle = A_2 + B_2 \ln\left(\frac{r'_0}{\eta_1}\right) + \frac{B_2}{r'_0} \mathrm{d}r' - \frac{B_2}{2r'^2_0} \left(\mathrm{d}r'\right)^2 + \cdots, \tag{2.14a}$$

$$\langle \Delta u^{+2} \rangle = 2\langle u^{+2} \rangle - D_2 \exp\left(-E_2 r'_0\right) + D_2 E_2 \exp\left(-E_2 r'_0\right) \mathrm{d}r' - \frac{D_2 E_2^2}{2} \exp\left(-E_2 r'_0\right) \left(\mathrm{d}r'\right)^2 + \cdots. \tag{2.14b}$$

Matching the leading, the first- and second-order terms at $r_0' = \eta_2$, we obtain

$$D_2 = B_2 \mathrm{e}, \tag{2.15a}$$

$$\eta_2 = \frac{1}{E_2} = \eta_1 \exp\left(\frac{2\langle u^{+2}\rangle - B_2 - A_2}{B_2}\right). \tag{2.15b}$$

Thus, (2.13) becomes

$$\langle \Delta u^{+2}\rangle = 2\langle u^{+2}\rangle - B_2 \exp\left(1 - \frac{r}{z\eta_2}\right), \quad \frac{r}{z} > \eta_2. \tag{2.16}$$

At the intermediate scale within distinct ranges, the dominant terms exhibit comparable magnitudes, while higher-order terms might also hold significance (Tong & Ding 2019). Here, to obtain a concise expression, we neglect these higher-order terms for simplicity and find that direct matching of low-order terms works well. Equations (2.10), (2.11) and (2.16) constitute the global expression for the second-order structure function, where the coefficients are not all independent. With known turbulent intensity $\langle u^{+2}\rangle$ and three small-scale parameters M_2, ξ_2 and η_1, the global expression for the second-order structure function is determined. For a fixed height, the global expression applied to three horizontal scale ranges is determined by four parameters: $\langle u^{+2}\rangle$, M_2, ξ_2 and η_1. Additionally, the height dependence is captured by the logarithmic dependence of $\langle u^{+2}\rangle$, $\langle u^{+2}\rangle = A_1 - B_1 \log(z/\delta)$, thus, we have in total five parameters: A_1, B_1, M_2, ξ_2 and η_1.

Assuming that the boundary layer thickness captures the outer scale for large-scale motions, we set the large-scale range's characteristic scale $\eta_2 z$ of $O(\delta)$. In the logarithmic region, the streamwise turbulence intensity follows (Marusic *et al.* 2013; Meneveau & Marusic 2013)

$$\langle u^{+2}\rangle = A_1 - B_1 \ln\left(\frac{z}{\delta}\right), \tag{2.17}$$

where B_1 is the Townsend–Perry constant and A_1 is a flow-dependent constant. The size of the attached eddies that contribute to the velocity ranges from z to δ, which is consistent with δ as the characteristic length scale of the large-scale range. Substituting (2.17) into (2.15*b*), we get

$$\eta_2 = \eta_1 C_\eta \left(\frac{\delta}{z}\right)^{2B_1/B_2}, \tag{2.18}$$

where $C_\eta = \exp[(2A_1 - B_2 - A_2)/B_2]$ and η_1 is of $O(1)$. Considering a canonical situation with $B_2 = 2B_1$ (Davidson *et al.* 2006*b*; Davidson & Krogstad 2014), for example, $B_1 = 1.25$ (Meneveau & Marusic 2013) and $B_2 = 2.5$ (Xie *et al.* 2021), we obtain $\eta_2 \sim \delta/z$, which is consistent with our analysis and the assumption that $\eta_2 z \sim \delta$. Also, rearranging (2.15*b*), we obtain

$$\langle u^{+2}\rangle = \frac{A_2 + B_2}{2} + \frac{B_2}{2} \ln\left(\frac{\eta_2}{\eta_1}\right). \tag{2.19}$$

Taking the approximation $\eta_2/\eta_1 \sim \delta/z$, (2.19) recovers the expression for streamwise turbulent intensity (2.17) and $B_2 = 2B_1$. Even though B_2 may not equal twice of B_1 in real ASL measurement data, which we show in figure 10(*b*) (§ 3.3), the assumed exponential expression in the large-scale range links the dynamic range and $r \to \infty$, and is consistent with the matching procedure by Davidson & Krogstad (2014). The above results show that the proposed exponential function for $\langle \Delta u^{+2}\rangle$ based on the ARMA model is consistent with and bridges previous theories.

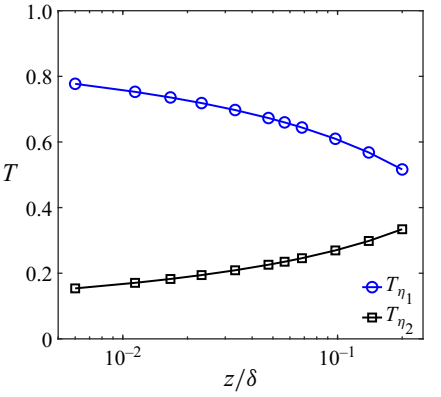

Figure 3. Variation of T_{η_1} and T_{η_2} with z/δ according to (2.21*a*) and (2.21*b*), where $M_2 = 3.62$, $B_1 = 1.25$, $A_1 = 1.73$ and $B_2 = 2.5$.

2.4. *Implication of the global expression*

2.4.1. *Characteristic length scales calculated from the global expression*

In this section, we derive the expression of characteristic length scale from the previously obtained expression of $\langle \Delta u^{+2} \rangle$. The characteristic length scale L_x is defined by introducing an artificial threshold T of the autocorrelation:

$$R_{uu}(L_x/2) = T\langle u^2 \rangle. \tag{2.20}$$

Though studies show that the threshold value does not change the trend of obtained length scales (Zhou *et al.* 1999), we believe the reason is that the threshold values are usually small. The length-scale behaviour could change when different thresholds locate in different ranges of the second-order structure function. For example, the thresholds corresponding to η_1 and η_2 are

$$T_{\eta_1} = 1 - \frac{M_2 \eta_1^{\xi_2}}{2\langle u^{+2} \rangle}, \tag{2.21a}$$

$$T_{\eta_2} = \frac{B_2}{2\langle u^{+2} \rangle}. \tag{2.21b}$$

The dependences of T_{η_1} and T_{η_2} on z/δ are shown in figure 3, showing that the detected characteristic length scale depends on the choice of the threshold value, e.g. if $T = 0.05$, the threshold locates in the large-scale range, and if $T = 0.4$, the threshold locates in the dynamic range.

Taking $\langle \Delta u^{+2} \rangle = 2(1-T)\langle u^{+2} \rangle$ in different ranges of $\langle \Delta u^{+2} \rangle$, we can obtain the analytical expression for the length scale L_x/δ predicted for different thresholds:

$$\frac{L_x}{\delta} = \begin{cases} 2\eta_1 C_\eta \left(\dfrac{z}{\delta}\right)^{1-2B_1/B_2} \left\{1 - \ln\left[\dfrac{2T}{B_2}\left(A_1 - B_1 \ln\left(\dfrac{z}{\delta}\right)\right)\right]\right\}, & T < T_{\eta_2}, \\ 2\eta_1 \exp\left[\dfrac{2(1-T)A_1 - A_2}{B_2}\right]\left(\dfrac{z}{\delta}\right)^{1-2B_1(1-T)/B_2}, & T_{\eta_2} < T < T_{\eta_1}, \\ 2\dfrac{z}{\delta}\left[\dfrac{2(1-T)}{M_2}\left(A_1 - B_1 \ln\left(\dfrac{z}{\delta}\right)\right)\right]^{1/\xi_2}, & T > T_{\eta_1}. \end{cases} \tag{2.22}$$

Since $\langle u^{+2}\rangle$ is expressed in terms of A_1 and B_1, there is an extra parameter in the expression for L_x compared with the global expression for the second-order structure function. The main independent parameters that control the behaviour of L_x are A_1/B_2 and B_1/B_2, and other parameters are close to their canonical value. It is interesting to show that when $T < T_{\eta_2}$, the characteristic length has a double-log dependence on the distance to the wall, which is one of our main results and is checked below by experimental data. Additionally, for a threshold value corresponding to the dynamic and inertial ranges, the behaviours of L_x can also be described by (2.22). If one wants to observe the large characteristic scales corresponding to the flow structure with the dynamics, the threshold value should not be chosen to be greater than the minimum value of T_{η_2}, as shown in figure 3.

2.4.2. *Lower bound for the streamwise turbulent intensity in the logarithmic region*
Assuming that the streamwise autocorrelation function decays with increasing scale, which is commonly found in experiments and numerical simulations of boundary-layer turbulence, the value of $\langle \Delta u^{+2}\rangle$ at $r/z = \eta_2$ should be larger than that at $r/z = \eta_1$ in the dynamic range. Therefore, (2.11) and (2.16) imply

$$2\langle u^{+2}\rangle - B_2 \geq A_2. \tag{2.23}$$

With $A_2 = B_2/\xi_2$ and $B_2 = C_2\kappa^{-2/3}\eta_1^{\xi_2}\xi_2$, we obtain

$$\langle u^{+2}\rangle \geq \frac{1}{2}\left(1 + \frac{1}{\xi_2}\right) C_2\kappa^{-2/3}\eta_1^{\xi_2}\xi_2. \tag{2.24}$$

Taking $C_2 = 2$, $\kappa = 0.4$, $\xi_2 = 2/3$ and $\eta_1 = 1$, we find a lower bound for the turbulence intensity in the logarithmic region $\langle u^{+2}\rangle \geq 3.07$, which is justified by previous results $\langle u^{+2}\rangle$ (Hutchins *et al.* 2012; Wang & Zheng 2016). In addition, this lower bound depends on the imbalance between energy production and dissipation because η_1 increases as dissipation increases (Zhang *et al.* 2022). More numerical and experimental results are needed to further check the validity of this lower bound.

2.4.3. *Estimation of the integral length scale*
Knowing the global expression for second-order structure function, the integral length scale $\mathcal{L}$ can be calculated as

$$\mathcal{L} = \int_0^\infty \frac{\langle u_1u_2\rangle}{\langle u^2\rangle}\,\mathrm{d}r = \int_0^\infty \frac{\langle u^2\rangle - \langle \Delta u^2\rangle/2}{\langle u^2\rangle}\,\mathrm{d}r = \int_0^\infty \left(1 - \frac{\langle \Delta u^{+2}\rangle}{2\langle u^{+2}\rangle}\right)\mathrm{d}r. \tag{2.25}$$

Denoting r/z as η, and using (2.10), (2.11) and (2.16), we get

$$\begin{aligned}\frac{\mathcal{L}}{z} &= \int_0^\infty \left(1 - \frac{\langle \Delta u^{+2}\rangle}{2\langle u^{+2}\rangle}\right)\mathrm{d}\eta \\ &\approx \int_0^{\eta_1}\left(1 - \frac{M_2\eta^{\xi_2}}{2\langle u^{+2}\rangle}\right)\mathrm{d}\eta + \int_{\eta_1}^{\eta_2}\left[1 - \frac{A_2 + B_2\ln(\eta/\eta_1)}{2\langle u^{+2}\rangle}\right]\mathrm{d}\eta \\ &\quad + \int_{\eta_2}^\infty \left[1 - \frac{2\langle u^{+2}\rangle - B_2\mathrm{e}^{1-\eta/\eta_2}}{2\langle u^{+2}\rangle}\right]\mathrm{d}\eta \\ &= I_1 + I_2 + I_3.\end{aligned} \tag{2.26}$$

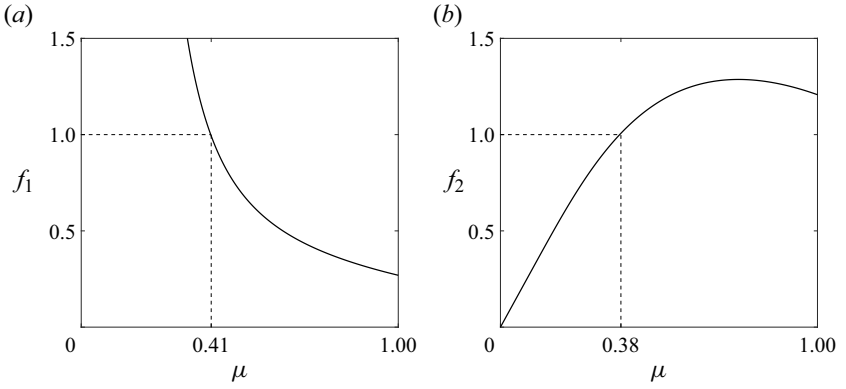

Figure 4. Variations of (*a*) f_1 and (*b*) f_2 with $\mu = B_2/(2\langle u^{+2}\rangle)$ for $\xi_2 = 2/3$.

Referring to (2.12*a*,*b*) and (2.15*b*), we can express M_2, A_2 and η_2 as functions of B_2, η_1 and ξ_2. Denoting $B_2/(2\langle u^{+2}\rangle)$ as μ, the integrals in (2.26) can be calculated as

$$I_1 = \int_0^{\eta_1} \left(1 - \frac{\mu\eta^{\xi_2}}{\eta_1^{\xi_2}\xi_2}\right) \mathrm{d}\eta = \eta_1 - \frac{\mu}{\xi_2(\xi_2+1)}\eta_1, \tag{2.27a}$$

$$I_2 = \int_{\eta_1}^{\eta_2} \left[1 - \frac{\mu}{\xi_2} - \mu \ln\left(\frac{\eta}{\eta_1}\right)\right] \mathrm{d}\eta = \left(\frac{\mu}{\xi_2} - 1 - \mu\right)\eta_1 + 2\mu\eta_2, \tag{2.27b}$$

$$I_3 = \int_{\eta_2}^{\infty} \left[\mu \mathrm{e}^{1-\eta/\eta_2}\right] \mathrm{d}\eta = \mu\eta_2, \tag{2.27c}$$

where the second integral uses $\ln(\eta_2/\eta_1) = 1/\mu - 1 - 1/\xi_2$ (cf. (2.15*b*)). Then we obtain

$$\frac{\mathcal{L}}{z} = -\frac{\xi_2\mu}{\xi_2+1}\eta_1 + 3\mu\eta_2. \tag{2.28}$$

Again using (2.15*b*), (2.28) can be further expressed as

$$\frac{\mathcal{L}}{z} = \left[3\mu \exp\left(\frac{1}{\mu} - 1 - \frac{1}{\xi_2}\right) - \frac{\xi_2\mu}{\xi_2+1}\right]\eta_1 = f_1(\mu,\xi_2)\eta_1 \tag{2.29a}$$

or

$$\frac{\mathcal{L}}{z} = \left[3\mu - \frac{\xi_2\mu}{(\xi_2+1)\exp(1/\mu - 1 - 1/\xi_2)}\right]\eta_2 = f_2(\mu,\xi_2)\eta_2. \tag{2.29b}$$

Here, the expressions are reformed to compare with two characteristic scales corresponding to η_1 and η_2. The values of f_1 and f_2 with $\xi_2 = 2/3$ are shown in figure 4. The parameter μ that guarantees $f_1 > 1$ and $f_2 < 1$ is often achieved in boundary-layer turbulence, e.g. with $B_2 = 2.36$ and the lower bound of streamwise turbulent intensity $\langle u^{+2}\rangle \geq 3.07$ estimated in § 2.4.2. Therefore, in the logarithmic region, the integral length scale $\mathcal{L}$ locates in the dynamic range, which is consistent with $\mathcal{L}$ estimated in the neutral ASL and experiments (Hutchins & Marusic 2007; Gustenyov *et al.* 2023).

Throughout the remainder of the article, we apply the ARMA(1, q) model on the streamwise velocity of ASL turbulence and test our theoretical expressions (2.16), (2.22) and (2.29) at $Re_\tau \sim O(10^6)$.

3. Application to the ASL data

3.1. *Experimental facility and data pretreatment*

The ASL data used in this work come from QLOA, which is built on the flat dry lakebed of Qingtu Lake in western China (E: 103°40′03″, N: 39°12′27″) and provides the highest order of magnitude friction Reynolds number data to date. Also, QLOA is the unique observation site where multi-point measurements can be performed simultaneously, including three-dimensional turbulent velocities, temperature, humidity, PM10 concentration and electric field, and so forth. The high-quality data of clear-air and sand-laden ASL flows proved suitable for turbulent boundary layer studies (Wang & Zheng 2016; Liu, Wang & Zheng 2019*a*; Wang, Gu & Zheng 2020; Liu, He & Zheng 2021). The main tower is 32 m high and has measurement positions at 0.9, 1.71, 2.5, 3.49, 5, 7.15, 8.5, 10.24, 14.65, 20.96 and 30 m, approximately logarithmically aligned. Eight low towers of 5 m high are arranged at an equal distance of 30 m in the prevailing wind direction, and twelve low towers of 5 m high are arranged at an equal distance of 5 m in the spanwise direction. The data used in this study were obtained from the main tower, whose height lies roughly in the logarithmic region of the atmospheric boundary layer. The three-component sonic anemometers (Campbell scientific, CSAT-3B) installed on the tower measure the velocities and temperature synchronously, with a sampling frequency of 50 Hz, a velocity measurement range of 0–45 m s^{-1}, a minimum velocity resolution of 0.001 m s^{-1}, a temperature measurement range of −40–60 °C, a minimum temperature resolution of 1 °C and a wind direction recording range of 0–359°. The sonic anemometers are all connected to data acquisition instruments that are time-synchronized with the global positioning system to ensure data synchronization.

Due to the uncertainty and uncontrollability of field measurement, the measured data need to be selected and pretreated. The same pretreatment procedures as previous ASL turbulence studies using QLOA data are implemented here. The raw data are partitioned into hourly time series, and then the pretreatments including wind direction adjustment, detrending manipulation, stratification stability judgment and stationary wind selection is carried out. Although the streamwise direction of QLOA is designed to be consistent with the prevailing wind direction, the wind direction changes during the field measurement. So the measured data need to be adjusted as

$$u = u_m \cos\omega + v_m \sin\omega, \quad v = v_m \cos\omega - u_m \sin\omega, \tag{3.1a,b}$$

where u_m and v_m are streamwise and spanwise velocities measured by the anemometers, and ω is the angle between the actual wind direction and the streamwise direction of QLOA averaged over all heights. After adjusting the wind direction, the long-term synoptic signal also needs to be detrended by a low-pass filter with a cut-off wavelength of 20δ to extract the turbulence fluctuating signal.

In addition, thermal convection often occurs in ASL turbulence, affecting the budget of turbulent kinetic energy (Wyngaard & Coté 1971; Wyngaard, Coté & Izumi 1971). The Monin–Obukhov stratification parameter (Monin & Obukhov 1954), which characterizes the ratio of the buoyancy and shear effects, is often used to evaluate the stratification conditions and is defined as

$$\frac{z}{L} = -\frac{\kappa z g \langle w\theta \rangle}{\langle \theta \rangle u_\tau^3}, \tag{3.2}$$

where L is the Obukhov length (Obukhov 1946), g is the acceleration of gravity, and $\langle w\theta \rangle$ is the mean vertical heat flux defined as the covariance of the vertical wind velocity w and the measured potential temperature θ. If $|z/L| \ll 1$, the ASL flow is shear-dominant

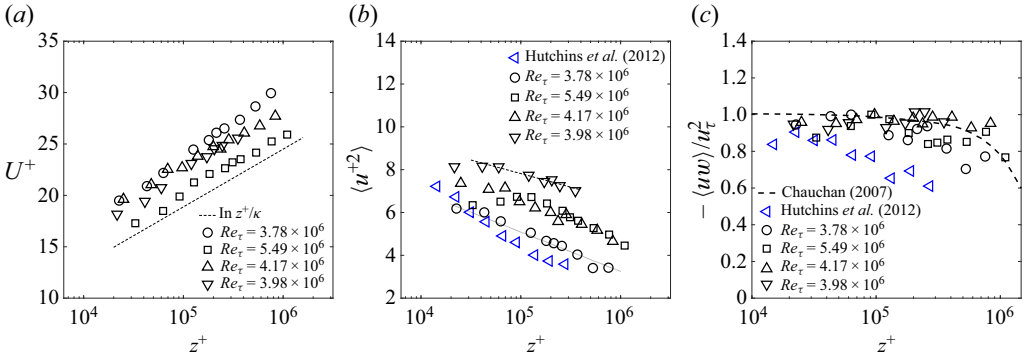

Figure 5. Profiles of statistics for selected intervals at $Re_\tau = O(10^6)$. (*a*) Log-linear plot of the mean streamwise velocity. The open symbols are current QLOA data and the dashed line corresponds to the log-law with $\kappa = 0.41$ (Pope 2000). (*b*) Logarithmic decay of streamwise turbulent intensity. The blue symbols is the ASL result of Hutchins *et al.* (2012) at $Re_\tau = O(10^6)$. The dashed and dotted lines correspond to (2.17) with $B_1 = 0.55$ and 0.80, respectively. (*c*) Dimensionless shear Reynolds stress. The blue symbols are ASL data from Hutchins *et al.* (2012) and the dashed line is the similarity formulation from Chauhan (2007).

and the density stratification is negligible. In our analysis, the Monin–Obukhov stability parameter is calculated at $z = 1.71$ m, and we select the near-neutral data with $|z/L| < 0.06$. Another effective indicator of the stratification stability is the $k_x^{-5/3}$ scaling of spectra at low wavenumber (Tong & Nguyen 2015; Tong & Ding 2019). If the k_x^{-1} scaling is observed instead of $k_x^{-5/3}$, the ASL flow can be considered to be shear dominant and therefore near-neutral. The streamwise spectra of the ASL data used in this work exhibit no significant $k_x^{-5/3}$ range at low wavenumber, as shown, for example, in figure 9(*a*) (§ 3.2).

Since we focus on fully developed stationary turbulence, selecting the statistically stationary ASL data is necessary. A non-stationary index γ is used to judge the stationarity, which is defined as

$$\gamma = |(\sigma_M - \sigma_I)/\sigma_I| \times 100\,\%, \tag{3.3}$$

where $\sigma_M = \sum_{i=1}^{12} \sigma_i/12$, $\sigma_1, \sigma_2, \ldots, \sigma_{12}$ are the streamwise velocity variances of one-twelfth part of the entire time interval and σ_I is the variance of the overall time interval. Stationarity requires ASL data over the interval to meet $\gamma < 30\,\%$ and we pick the half-hour with the smallest γ in an hour as our time interval.

Other quantities used here are defined as follows, consistent with previous studies at the QLOA site under the near-neutral stratification conditions. The friction velocity u_τ is approximated by the peak value of $(-\langle uw\rangle)^{1/2}$. The air kinematic viscosity ν is calculated from the measured mean temperature under standard atmospheric pressure. Additionally, the ASL thickness δ is estimated as 150 m to evaluate the friction Reynolds number Re_τ. Some basic flow information of the selected intervals, including the mean velocity profile, the streamwise turbulent intensity and the shear Reynolds stress, are shown in figure 5. Comparison with ASL data obtained by Hutchins *et al.* (2012) and theoretical results of boundary-layer turbulence proves that our data are consistent with the logarithmic region of the boundary layers.

3.2. *Justifying the ARMA model*

In this section, we justify that the ARMA model can well capture the second-order statistics of the ASL data in the dynamic and large-scale ranges. The procedural workflow

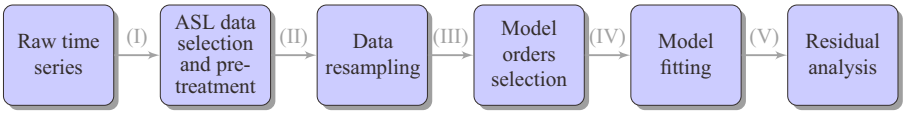

Figure 6. Diagrammatic flow of applying the ARMA model to boundary-layer turbulence.

for applying the ARMA model to boundary-layer turbulence is visually depicted in figure 6. (I) In the first step, ASL data selection and pretreatment are performed. These details are described in § 3.1. (II) Once the streamwise velocity series is obtained, we need to determine two characteristic scales η_1 and η_2. Based on AEM, we have $\eta_1 = O(1)$, so we choose the interval for the extracted velocity series as $\Delta t/\Delta t_0 = z/(U\Delta t_0)$. This resampling process filters out the inertial range. (III) In § 2.1, we specify the model orders as $p = 1$ and $q = \eta_2/\eta_1$. The largest scale η_2 of the dynamic range can be estimated by (2.15*b*). Alternatively, a more accurate approach to determine η_1 and η_2 is by obtaining η_1 from the inertial and dynamic ranges of the ASL data according to (2.10)–(2.11), and then calculating η_2 with the help of (2.15*b*). Specifically, the power fit for scale range less than η_1 yields M_2 and ξ_2, then A_2, B_2 and η_2 can be obtained by (2.12*a*,*b*) and (2.15*b*), and then it is convenient to optimize η_1 that minimizes the total absolute error of the global expression by the optimization method, such as the 'fmincon' function in MATLAB. We adopt the latter approach in this work. (IV) Knowing the value of η_1 and η_2, we can obtain q and use the ARMA(1, q) model to fit the extracted series. The fourth step uses the same approach as the statistical practice, which is available in many function packages, and here we use the 'arima' function in R. (V) After the model fitting procedure, an essential fifth step involves evaluating the model's goodness of fit. A common approach is to scrutinize the residuals resulting from the model fitting process; if these residuals exhibit characteristics akin to white noise, we validate the model. Conventional practices for this purpose encompass well-known statistical tests such as the Ljung–Box and Breusch–Godfrey tests (Liu, Erdem & Shi 2011). In the present study, the model residuals successfully pass the Ljung–Box test with a p-value larger than 0.05, indicating that the ARMA model captures the correlation of boundary-layer turbulence well.

There are two significant distinctions from traditional statistical practice in our procedure. First, the precondition of stationarity is required before employing the ARMA model. The traditional statistical modelling methods require only the removal of mean value by applying a moving average or a differential operator and the removal of periodic signals. Considering the physics of the ASL, we also need to ensure neutrality and filter large-scale synoptic signals. Second, the typical approach for ascertaining the model orders involves statistical criteria such as the Akaike or Bayesian information criterion (Choi 2012). In contrast, within this study, we establish the model order based on the characteristic scale of the boundary layer, which again is restricted to ASL physics. This approach enhances the model's interpretability and endows the model with heightened physical significance.

Figure 7 shows an example of fitting the ARMA model. The half-hour raw fluctuating velocity series is presented in figure 7(*a*). Additionally, the reproduced coarse series is shown in figure 7(*b*). Using the ARMA model, we can regenerate the velocity series with almost the same velocity variance of raw data. Moreover, compared with the autocorrelation calculated from raw data, the autocorrelation generated by the ARMA(1, q) model fits well, which is shown in figure 7(*c*). Figure 7(*d*) shows the corresponding second-order structure function, and the consistency between the result of the ARMA

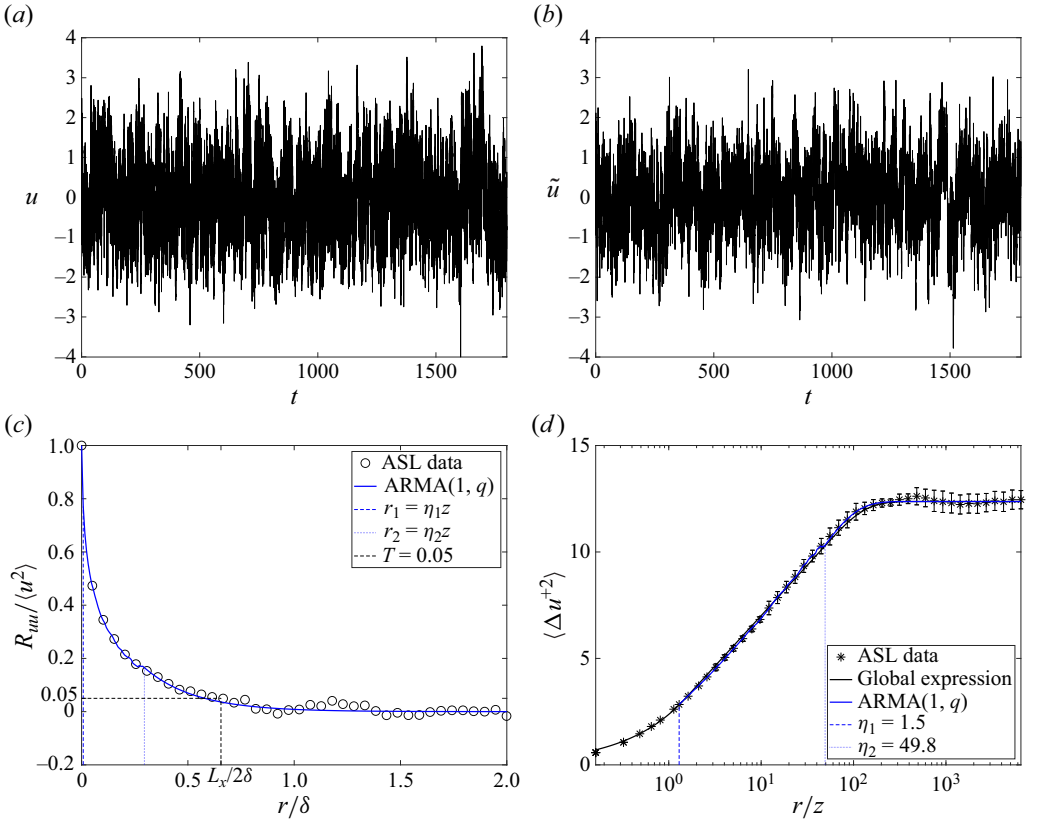

Figure 7. (*a*) Raw fluctuating velocity u; (*b*) reproduced fluctuating velocity $\tilde{u}$; (*c*) comparison of autocorrelations of ASL data and ARMA model in normal-normal coordinates; and (*d*) comparison of the global expression, second-order structure functions of ASL data and ARMA model in log-normal coordinates, where $u_\tau = 0.37$ m s^{-1}, $Re_\tau = 3.78 \times 10^6$ and $z^+ = 2.27 \times 10^4$.

model and the proposed global expression indicates the validity of the approximate exponential function in the large-scale range. These results validate the applicability of using the ARMA(1, q) model to describe the boundary-layer streamwise velocity series.

As discussed in § 2.1, we simplify the attached eddies with continuously varying sizes to a series of eddies whose sizes are approximated as a multiple of z up to δ. The model parameters β_i quantify these attached eddies' effects on the current position's acceleration. Figure 8(*a*) shows that at all heights, as the distance $i\Delta x$ increases, the effect of corresponding attached eddies (β_i^2) decreases, indicating that the attached eddies with larger size contribute less to the fluctuating velocity. In addition, the model's memory depth is restricted to the dynamic range, where autocorrelation shows a logarithmic behaviour. Figure 8(*b*) shows that the self-similar random effect with a -2 power scaling of β_i leads to a logarithmic autocorrelation, which is discussed in detail in Appendix B.

Here, the ARMA(1, q) model is used to model the dynamic range and to obtain the large-scale range's behaviour as a natural extension. To justify the large-scale behaviour, in figure 9, we show the premultiplied spectra, whose peak is used to distinguish large- and very-large-scale motions (Wang & Zheng 2016). Even though small scales are not resolved by the ARMA(1, q) model, its premultiplied spectra well captures that of the ASL data. Note that since the one-dimensional spectra at low wavenumber contain

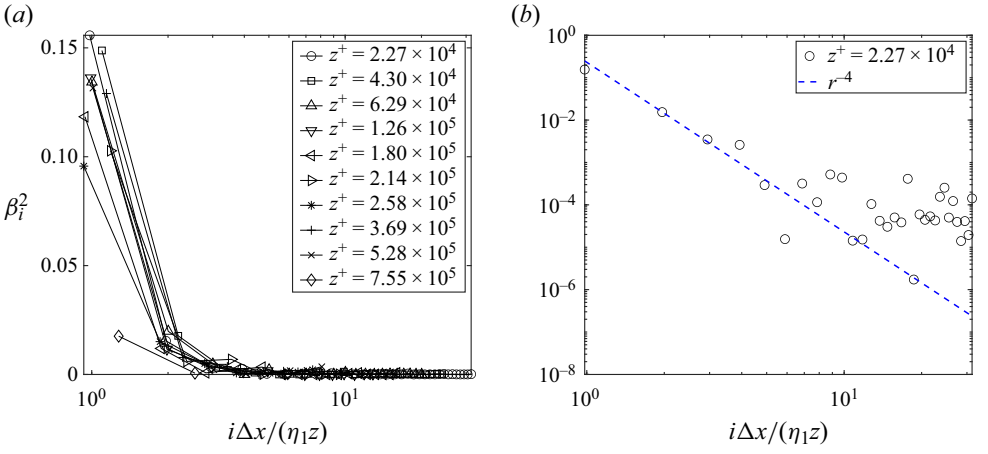

Figure 8. Fitted model parameters β_i, $i = 1, 2, \ldots, q$, with $Re_\tau = 3.78 \times 10^6$.

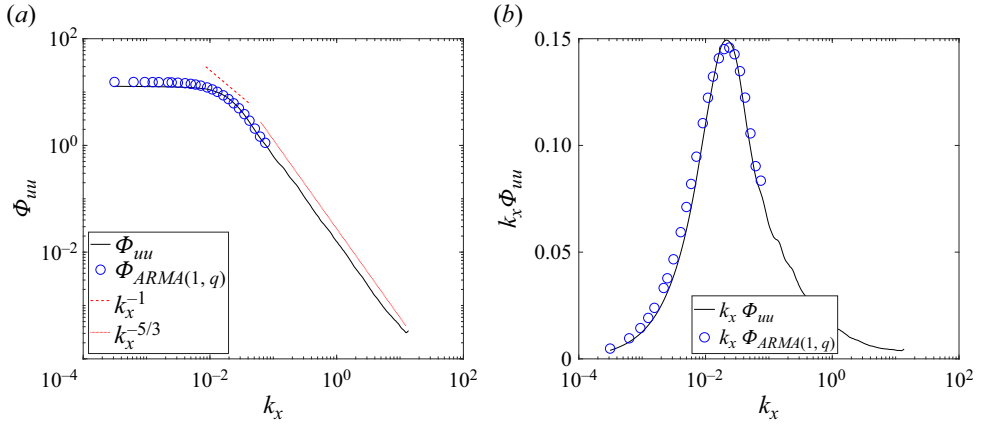

Figure 9. (*a*) Power spectra Φ_{uu} and (*b*) premultiplied spectra $k_x\Phi_{uu}$ obtained from ASL data and ARMA(1, q) model, respectively. Here $Re_\tau = 3.78 \times 10^6$ and $z^+ = 7.55 \times 10^5$.

an aliasing effect, one needs to be careful when examining large-scale information from one-dimensional spectra. Improved approaches include examining two-dimensional spectra (Tong & Nguyen 2015) and employing Fourier cutoff techniques (Ding *et al.* 2018).

3.3. *Asymptotic global expression of the second-order structure function*

Because the exact expression of the second-order structure function calculated from the ARMA(1, q) model is complicated, for analytic simplicity, we derive a global asymptotic expression for the second-order structure function $\langle \Delta u^{+2} \rangle$ in § 2.3 (cf. (2.10), (2.11) and (2.16)), which is justified in figure 10(*a*). The uncertainty ranges of parameters M_2, ξ_2 and η_1 are discussed in Appendix C. Additionally, η_2 is calculated from (2.15*b*) with the optimized η_1. The parameters of inertial and dynamic ranges are close to the results of de Silva *et al.* (2015).

According to (2.18), η_2/η_1 is a power function of z/δ, which we check in figure 10(*b*). This exponent is conventionally regarded to be 1, corresponding to the empirical values

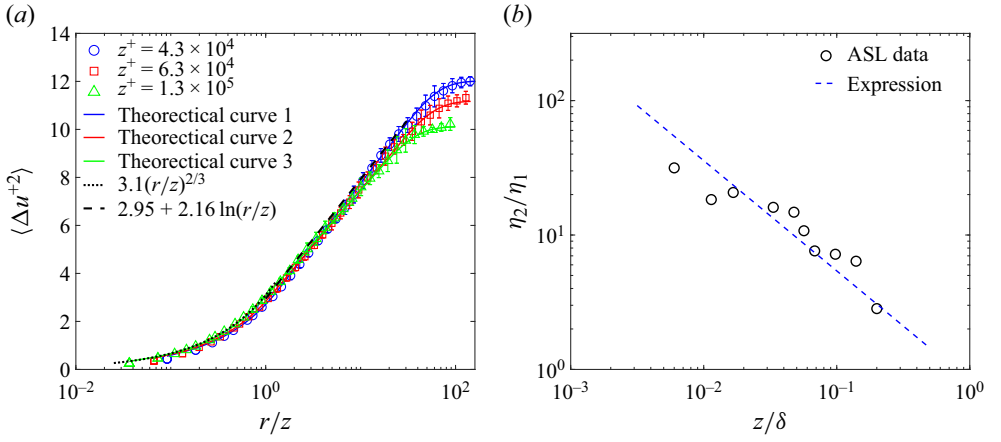

Figure 10. (*a*) Comparison of $\langle \Delta u^{+2} \rangle$ obtained from ASL data and global asymptotic expression at $Re_\tau = 3.78 \times 10^6$. The intermediate scales of theoretical curves are as follows: Curve 1 – $\eta_1 = 1.06$, $\eta_2 = 27.71$; Curve 2 – $\eta_1 = 0.87$, $\eta_2 = 23.12$; Curve 3 – $\eta_1 = 0.73$, $\eta_2 = 15.42$. The black curves correspond to expressions for inertial and dynamic ranges presented by de Silva *et al.* (2015). (*b*) Comparison of η_2 obtained from ASL data and the expression (2.18) with $A_1/B_2 = 1.15$, $A_2/B_2 = 1/\xi_2 = 1.50$, $B_1/B_2 = 0.41$ and $B_1 = 0.80$.

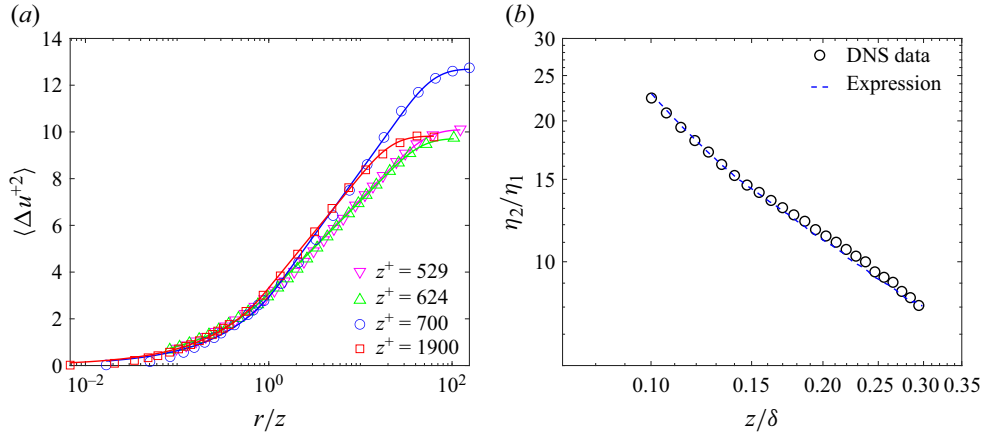

Figure 11. (*a*) Comparison of $\langle \Delta u^{+2} \rangle$ obtained from DNS and experiment data and global asymptotic expression. Here, z^+ locates in the logarithmic region. The triangle symbols correspond to the DNS data at $Re_\tau \approx 5200$ (Lee & Moser 2015), and the circle and square symbols correspond to the experiment data $Re_\tau = 19\,000$ (Hutchins *et al.* 2009; de Silva *et al.* 2015). (*b*) Comparison of η_2 obtained from DNS data and the expression (2.15*b*) with $A_1 = 1.72$ and $B_1 = 1.50$.

of $B_1 = 1.25$ and $B_2 = 2.5$. However, in ASL data, B_1 often deviates from 1.25, and some researchers argue that B_1 may decrease with increasing Re_τ (Monkewitz 2022). In addition, B_2 depends on η_1 (cf. (2.11)), which is influenced by the ratio between the energy production and dissipation rate. So instead of restricting the values of B_1 and B_2 individually, we take the realistic values obtained from ASL data to test our expressions.

Furthermore, we undertake validation of the global expression through direct numerical simulation (DNS) and experimental results. Illustrated in figure 11(*a*), the triangle symbols correspond to the DNS data at $Re_\tau \approx 5200$ obtained from Johns Hopkins turbulence database (Lee & Moser 2015). Although the logarithmic slope B_2 of DNS data ranges from

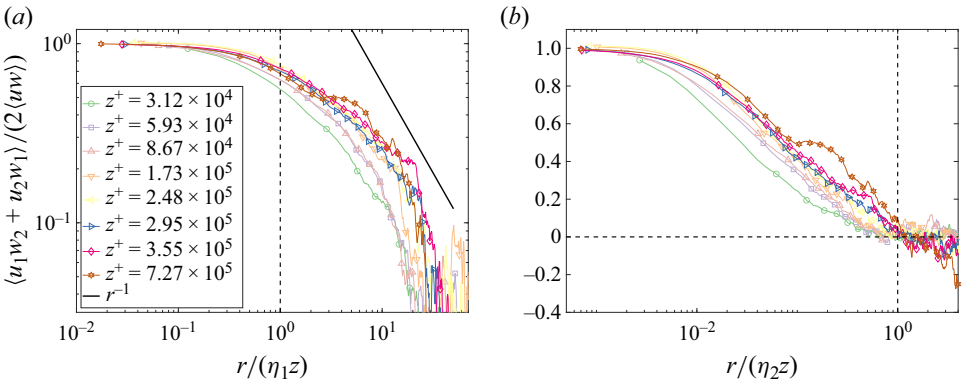

Figure 12. Behaviour of covariance of streamwise velocity u and vertical velocity w in the (a) dynamic range and (b) large-scale range.

1.46 to 1.78, smaller than the previously reported range of 2.16 to 2.5, the global expression matches the data well. The circle and square symbols in figure 11(a) correspond to the experiment results at $Re_\tau = 19\,000$, as detailed by Hutchins *et al.* (2009) and portrayed in figure 3(a) of de Silva *et al.* (2015). Combining these results from experiment, DNS and ASL data, we conclude that the proposed global expression for the second-order structure function is applicable across friction Reynolds numbers from $O(10^4)$ to $O(10^6)$. Since B_2 varies significantly with z^+ in DNS data, it is more appropriate to check (2.15b) rather than (2.18). The relationship between η_2 and η_1 obtained by asymptotic matching conforms well to the data, as shown in figure 11(b).

Introducing the two matching scales η_1 and η_2 makes a more lucid examination of behaviours across distinct scale ranges feasible. Within the transport equation for the second-order structure function, the shear production term $\langle \Delta u \Delta w\rangle \, \mathrm{d}U/\mathrm{d}z$ injects energy into the shear boundary layers. So we explore the scaling behaviour of $\langle u_1w_2 + u_2w_1\rangle$. Figure 12($a$) shows that the energy flux remains relatively constant within the inertial range (scales less than $\eta_1 z$). Additionally, in the dynamic range, $\langle u_1w_2 + u_2w_1\rangle$ follows a -1 power law that leads to the logarithmic expression for the structure functions (Xie *et al.* 2021). Conversely, scales exceeding $\eta_2 z$ exhibit negligible production. So $\eta_2 z$ is an approximate indicator of the energy injection scale in boundary layers. With negligible energy flux, the autocorrelation in the active range decays exponentially.

One main result of the present study is obtaining the expression of the second-order structure function in the large-scale range, which is beyond previous works on the inertial and dynamic ranges (Davidson *et al.* 2006*b*; Davidson & Krogstad 2014; de Silva *et al.* 2015). In our extended expression, the upper bound of the dynamic range scales as η_2. Thus, with scale normalized by $\eta_2 z$, collapse of data of different Re_τ in figure 13(a) justifies this characteristic scale. In the large-scale range, the exponential expression of the second-order structure functions obtained from the ARMA(1, q) model is justified in figure 13(b).

3.4. *The characteristic length scale*

The asymptotic global expression for the second-order structure function provides a theoretical expression for characteristic length scales L_x identified by a threshold of autocorrelation. The well-fitting result of the global expression implies the validity of (2.22). There are three independent parameters in (2.22): η_1, A_1/B_2 and B_1/B_2.

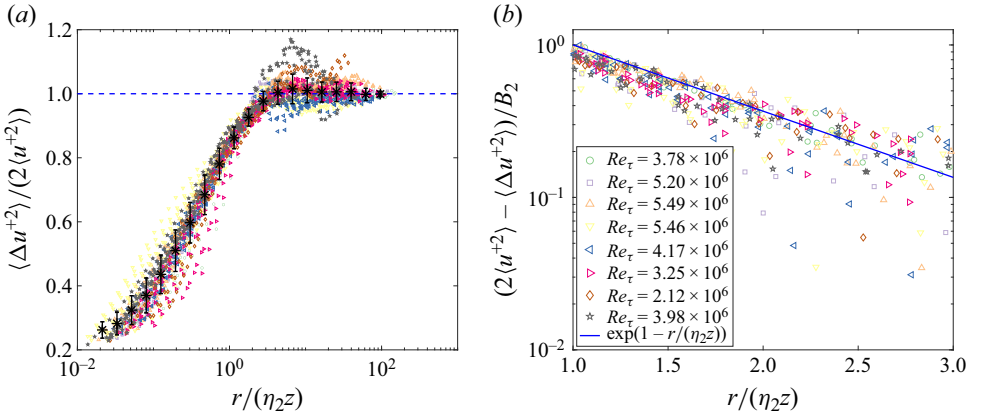

Figure 13. (*a*) Dynamic and large-scale ranges of second-order structure function with new scale $\eta_2 z$ at different high friction Reynolds numbers Re_τ. (*b*) Exponential scaling of the second-order structure function for scales larger than $\eta_2 z$.

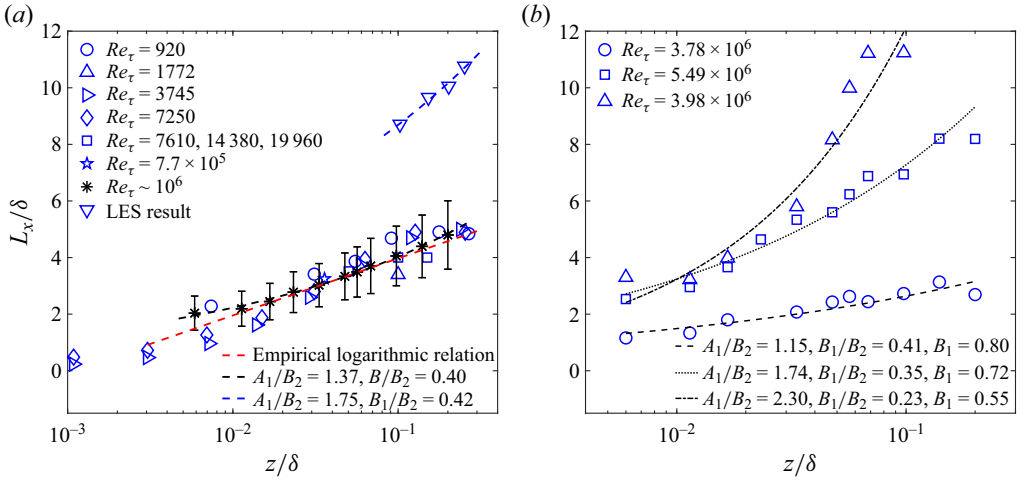

Figure 14. (*a*) Characteristic length scales summarized by Liu *et al.* (2017) and the data comes from Lee & Sung (2011), Volino, Schultz & Flack (2007), Tutkun *et al.* (2009), Hutchins & Marusic (2007), Hutchins *et al.* (2012), Liu *et al.* (2017) and Önder & Meyers (2018). Equation (2.22) provides the prediction of parameters A_1/B_2 and B_1/B_2. (*b*) Some ASL data that deviate from the L_x summarized by Liu *et al.* (2017) can also be characterized by (2.22). The height-averaged ratio of energy production and dissipation rate P/ε for the time intervals corresponding to the circle, triangle and square symbols are 1.84, 1.47 and 1.37, respectively.

The empirical scale η_1 and already defined constants A_1/B_2 and B_1/B_2 characterize the variation of L_x. As shown in figure 14(*a*), the previous results of L_x are summarized by Liu *et al.* (2017) with an approximate logarithmic expression. However, other studies found anomalous behaviour of L_x (Önder & Meyers 2018), suggesting that L_x may be variant under different flow conditions. Our double-log expression (2.22) with turning parameters well captures all data, implying it as a robust relation.

To further justify (2.22), in figure 14(*b*), we select three sets of ASL data with abnormal L_x. Equation (2.22) also describe these behaviours with parameters A_1/B_2 and B_1/B_2 obtained from the streamwise fluctuating velocity variance and second-order structure

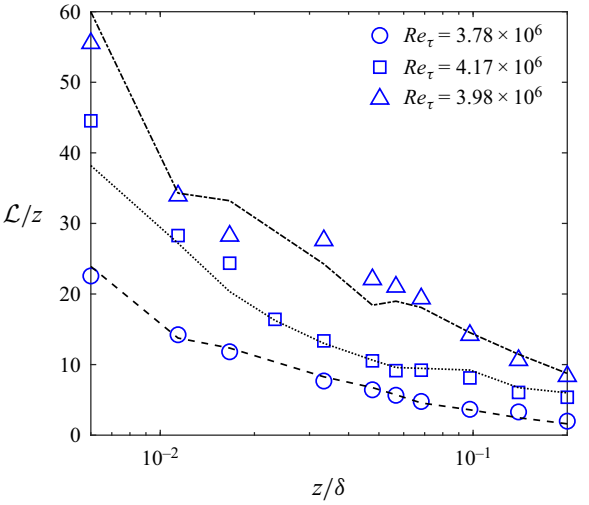

Figure 15. Comparison of integral length scale $\mathcal{L}$ and approximate expression (2.29*a*). The autocorrelation is integrated up to the first 0.01 crossing. The parameter μ in f_1 is obtained from ASL data and $\xi_2 = 2/3$.

function of the corresponding data sets. Note that in (2.22), in addition to A_1/B_2 and B_1/B_2, there is another parameter η_1 that needs to be determined, which is of order unity. In figure 14(*a*), η_1 is assumed to be 1 while it is taken as its average value at different heights in figure 14(*b*). The well-fitting results show that (2.22) is a good candidate to explain the variation of L_x.

Here our primary parameter of interest is B_1/B_2, which although has an accepted value of 0.5, deviates in different flows. As can be observed from the expression for L_x in the large-scale range (cf. (2.22)), the extent to which B_1/B_2 deviates from 0.5 leads mainly to the growth rate of L_x/δ with z/δ. Figure 14(*b*) shows that, usually, a smaller value of B_1/B_2 corresponds to a larger set of L_x/δ. In uncontrollable ASL measurements, flow parameters that deviate from the standard zero-pressure-gradient boundary layer are not rare, e.g. production and dissipation are not locally balanced, and the height dependence of turbulent kinetic energy can vary (cf. (2.17)). The unbalanced energy production and dissipation affects the intermediate scale η_1 between inertial and dynamic ranges (Zhang *et al.* 2022), thus impacting the value of L_x.

With the global expression, we can estimate the integral length scale $\mathcal{L}$ approximately. For ASL data, because errors at large scales have a significant impact on the calculation of $\mathcal{L}$, we integrate the dimensionless autocorrelation up to the first 0.01 crossing scale, similar to the approach adopted by O'Neill *et al.* (2004) and Tritton (2012). As shown in figure 15, (2.29*a*) characterizes the variation of $\mathcal{L}$ well. Since f_1 is sensitive to the value of μ, see figure 4, we determine the value of μ from ASL data rather than using empirical values and the small-scale power exponent is set as $\xi_2 = 2/3$. Additionally, as discussed in § 2.4.3, (2.29) indicates that $\mathcal{L}$ locates in the dynamic range, suggesting that $\mathcal{L}$ is a characteristic scale of the attached eddies in the logarithmic region.

4. Summary and discussion

To model the streamwise velocity and explore the autocorrelation in boundary-layer turbulence, we apply the ARMA model to the dynamic and large-scale ranges of the second-order structure function. Consistent with the knowledge of boundary-layer

turbulence and AEM, the memory depth q in the ARMA(1, q) model is determined by the lower and upper end of the dynamic range normalized by z, η_1 and η_2, respectively. The MA random effect in the ARMA(1, q) model dominates the behaviour of the dynamic range. A logarithmic second-order structure function is obtained when the randomness is self-similar, whose strength is captured by a power function with exponent -2. Additionally, we may regard the ARMA model as a stochastic AEM by the analogous linear additive random effects.

The ARMA model provides a natural extension of the second-order structure-function expression to the large-scale range (scales larger than $\eta_2 z$), where the autocorrelation of streamwise velocity decays exponentially. We match the expression for the dynamic range and an exponential expression at η_2 to the second-order derivative to obtain an approximate global expression for the second-order structure function $\langle \Delta u^{+2} \rangle$ (cf. (2.10), (2.11) and (2.16)). In the global expression, the large- and small-scale coefficients are connected by asymptotically matching at characteristic scales η_1 and η_2. For example, for inertial and dynamic ranges, only three of the five coefficients (M_2, ξ_2, η_1, A_2 and B_2) of the second-order structure-function expression are free and the global expression is determined after additionally determining the streamwise turbulence intensity $\langle u^{+2} \rangle$. This global expression is checked to be robust by well capturing the measured ASL data with non-canonical conditions and is applicable across friction Reynolds number from $O(10^4)$ to $O(10^6)$. Despite errors in autocorrelation and second-order structure function at large scales, the proposed expression yields an accurate calculation of the maximum energy injection scale η_2 and provides a method for determining the characteristic scale of the dynamic range from the streamwise turbulent intensity. These characteristic scales are relevant to other length scales in boundary-layer turbulence, as studied by Gustenyov *et al.* (2023). For example, in the near-wall region, the energetic scale approximates the upper bound of the inertial range, which is close to the scale $\eta_1 z$. Additionally, the interface wavelength quantifying the average distance between two near turbulent regions corresponds to the peak of premultiplied spectra, which is consistent with $\eta_2 z$, indicating that in ASL, the large-scale range may be affected by the non-turbulent external atmospheric environment.

Based on the expression of $\langle \Delta u^{+2} \rangle$, the expression for the streamwise characteristic scale L_x is obtained. When the threshold of the autocorrelation locates in the large-scale range, the ARMA model implies that the characteristic scale has a double-log dependence on the distance to the wall, which resembles the traditional log-dependence in the parameter regimes with local energy production–dissipation balance and $B_1/B_2 \approx 0.4$. In addition, our expression is also valid for non-standard situations, which is justified using ASL data with the Townsend–Perry constant and the logarithmic slope of $\langle \Delta u^{+2} \rangle$ deviating from their standard values. Thus, the robustness of this expression implies that the ARMA model captures certain underlying mechanisms in boundary-layer turbulence.

The exponential form of $\langle \Delta u^{+2} \rangle$ based on the ARMA model, which links the dynamic range and the infinitely large scale, can be used to explain the previously proposed relation that the logarithmic slope of $\langle \Delta u^{+2} \rangle$ is twice that of the streamwise turbulent intensity $\langle u^{+2} \rangle$ in the logarithmic region. For instance, Davidson *et al.* (2006*b*) matched the dynamic range with the expression for streamwise turbulence intensity directly to obtain

$$\langle \Delta u^{+2} \rangle (r) = A_2 + B_2 \ln (r/z), \quad z < r \ll \delta, \tag{4.1a}$$

$$\langle \Delta u^{+2} \rangle = 2\langle u^{+2} \rangle = 2\left[A_1 + B_1 \ln (\delta/z)\right], \quad r \sim \delta, \tag{4.1b}$$

where the coefficients B_2 in (4.1*a*) and $2B_1$ in (4.1*b*) are equal. This matching procedure assumes that the logarithmic behaviour of $\langle \Delta u^{+2} \rangle$ lasts to the scale of $r = O(\delta)$ and that the the autocorrelation at $r = O(\delta)$ is negligible so $\langle \Delta u^{+2} \rangle \approx 2\langle u^{+2} \rangle$. However, without an expression for the range $r \geq O(\delta)$, the validity of the above assumptions is not solid. Additionally, based on the empirical value of L_x larger than δ, we know that when $r = \delta$, the second-order structure function is at least smaller than $1.9\langle u^{+2} \rangle$. By proposing an expression of the large-scale range of $\langle \Delta u^{+2} \rangle$ using the ARMA model, we find when η_2/η_1 approximates δ/z, their procedure is valid (cf. (2.19)), while for other cases, the double relation between B_1 and B_2 is modified.

Also, we obtained a lower bound of $\langle u^{+2} \rangle$ in the logarithmic region, which is consistent with the existing numerical and experimental results (Hutchins *et al.* 2012; Wang & Zheng 2016). A dependence of this lower bound on the ratio of energy production to dissipation is proposed but remains to be checked. The global expression also yields an estimation of the integral length scale $\mathcal{L}$ (cf. (2.29)), which agrees well with the ASL data. Additionally, we conclude that in the logarithmic region of boundary-layer turbulence, $\mathcal{L}$ locates in the dynamic range of structure function and is a characteristic scale of attached eddies. A statistical study with more ASL data may be able to better validate (2.29*a*). In future studies, the same analytical procedure can be applied to the spanwise and wall-normal velocity series to explore the variation pattern of the corresponding characteristic length scales. Additionally, we can apply the ARMA(p, q) model with $p > 1$. For the multivariate case, the vector ARMA model may be used to detect spatial information such as the inclination angle of coherent structures (Li *et al.* 2022). For convective ASL, a new range emerges due to the buoyancy effect, as delineated by the multi-point Monin–Obukhov similarity theory (Tong & Nguyen 2015), and the combination of ARMA model and tempered fractional derivative (Samiee, Akhavan-Safaei & Zayernouri 2022) has the potential to capture the multi-scaling behaviour of structure functions.

Data errors and some assumptions limit the validation of present results. (i) The wall shear stress is not directly measured in QLOA and therefore the friction velocity u_τ is approximated by the shear Reynolds stress. (ii) The orders of the ARMA model are all integers. Inevitably, errors are caused by extracting new series and implementing discrete models on continuous flow motion. (iii) Though we propose an approximate expression for $\langle \Delta u^{+2} \rangle$, its accuracy remains to be checked at large scales due to the error arising from Taylor's frozen hypothesis (He, Jin & Yang 2017). This hypothesis is the only valid method for the current data to convert temporal data to the spatial domain, which is a common practice for ASL data analysis. For spatial data, the reformulation of the ARMA model is straightforward by replacing temporal separations with spatial separations, and it has the potential to capture more accurate physical information by avoiding the error brought about by the application of Taylor's frozen hypothesis.

Acknowledgements. We acknowledge valuable discussion with Yating Wan and open access direct numerical simulation data from Johns Hopkins turbulence databases.

Funding. F.-C.Z. and J.-H.X. gratefully acknowledge the financial support from the National Natural Science Foundation of China under Grant Nos. 92052102 and 12272006, and Joint Laboratory of Marine Hydrodynamics and Ocean Engineering, Laoshan Laboratory under Grant No. 2022QNLM010201. S.X.C. gratefully acknowledges financial support from the National Natural Science Foundation of China Grant No. 12292983. X.Z. gratefully acknowledges financial support from the National Natural Science Foundation of China Grant No. 92052202.

Declaration of interests. The authors report no conflict of interest.

Author ORCIDs.
Fei-Chi Zhang https://orcid.org/0000-0002-0049-7729;
Jin-Han Xie https://orcid.org/0000-0003-0502-8662;
Song Xi Chen https://orcid.org/0000-0002-2338-0873;
Xiaojing Zheng https://orcid.org/0000-0002-6845-2949.

Appendix A. Theoretical properties of the ARMA model

For an ARMA(p, q) model expressed as

$$u_t = \sum_{i=1}^{p} \alpha_i u_{t-i\Delta t} + \sum_{j=1}^{q} \beta_j \epsilon_{t-j\Delta t} + \epsilon_t, \tag{A1}$$

or

$$A(\mathcal{B})u_t = B(\mathcal{B})\epsilon_t, \tag{A2}$$

where $\mathcal{B}$ is the time lag operators with lag Δt, i.e. $\mathcal{B}^i u_t = u_{t-i\Delta t}$, and A and B are linear operators defined as $A(\mathcal{B}) = 1 - \sum_{i=1}^{p} \alpha_i \mathcal{B}^i$ and $B(\mathcal{B}) = 1 + \sum_{j=1}^{q} \beta_j \mathcal{B}^j$, respectively. The time step Δt could be chosen as the time interval corresponding to the measurement frequency of the time series or an artificially selected time step. The model equation (A1) or (A2) constrains the velocity at the moment t to be influenced up to the velocities of the previous p time steps (AR part) and the random noises of the previous q time steps (MA part).

If the ARMA model can be applied to the time series, some restrictions must be satisfied. For example, if $\{u_t\}$ is a causal function of $\{\epsilon_t\}$, there exists

$$u_t = \psi_0 + \psi_1 \epsilon_{t-\Delta t} + \psi_2 \epsilon_{t-2\Delta t} + \cdots = \Psi(\mathcal{B})\epsilon_t, \tag{A3}$$

where the parameters should satisfy $\sum_{i=0}^{\infty} |\psi_i| < \infty$ or $\Psi(z) \neq 0$ for $|z| \leq 1$. Additionally, the series $\{u_t\}$ should be an invertible function of $\{\epsilon_t\}$, i.e.

$$\epsilon_t = \vartheta_0 + \vartheta_1 u_{t-\Delta t} + \vartheta_2 u_{t-2\Delta t} + \cdots = \Theta(\mathcal{B})u_t, \tag{A4}$$

where the parameters should satisfy $\sum_{i=0}^{\infty} |\vartheta_i| < \infty$ or $\Theta(z) \neq 0$ for $|z| \leq 1$. Also, the series is stationary if and only if $\Psi(z) \neq 0$ for $|z| = 1$.

A.1. *Autocorrelation*

Since the model equation is linear, some basic properties of the ARMA model can be expressed explicitly, such as the autocorrelation

$$R_{uu}(k\Delta t) = \langle u_t u_{t-k\Delta t} \rangle, \tag{A5}$$

where k is the number of time steps and the angular brackets denote the time average over t. Since (A1) is a linear equation and the white noise ϵ_t is temporal independent, the autocorrelation of u_t can be calculated directly as

$$R_{uu}(k\Delta t) = \sigma_\epsilon^2 \sum_{i=0}^{\infty} \varphi_i \varphi_{i+k}, \tag{A6}$$

where $\varphi_0 = \beta_0 = 1$, $\varphi_k = H(q-k)\beta_k + \sum_{i=1}^{min\{k,p\}} \alpha_i \varphi_{k-i}$. This is a convenient calculation method but without an explicit expression. An alternative method to obtain autocorrelation

is to exploit the independence of white noise:

$$R_{uu}(k\Delta t) = \langle u_t u_{t-k\Delta t}\rangle, \\ = \left\langle \left(\sum_{i=1}^{p}\alpha_i u_{t-i\Delta t} + \sum_{j=0}^{q}\beta_j\epsilon_{t-j\Delta t}\right)\left(\sum_{i=1}^{p}\alpha_i u_{t-k\Delta t-i\Delta t} + \sum_{j=0}^{q}\beta_j\epsilon_{t-k\Delta t-j\Delta t}\right)\right\rangle, \tag{A7}$$

where $\langle\sum_{i=1}^{p}\alpha_i u_{t-i\Delta t}\sum_{i=1}^{p}\alpha_i u_{t-k\Delta t-i\Delta t}\rangle$ can easily be obtained since $\langle u_{t-i\Delta t}u_{t-j\Delta t}\rangle = R_{uu}(|i-j|\Delta t)$, and $\langle\sum_{j=0}^{q}\beta_j\epsilon_{t-j\Delta t}\sum_{j=0}^{q}\beta_j\epsilon_{t-k\Delta t-j\Delta t}\rangle$ can be calculated since $\langle\epsilon_{t-i\Delta t}\epsilon_{t-j\Delta t}\rangle = \delta_{ij}\sigma_\epsilon^2$. For the other two terms, if $p \geq q$, the calculations are as follows:

$$\begin{aligned}&\left\langle\sum_{i=1}^{p}\alpha_i u_{t-i\Delta t}\sum_{j=0}^{q}\beta_j\epsilon_{t-j\Delta t}\right\rangle \\ &= \langle\alpha_1 u_{t-\Delta t}(\beta_1\epsilon_{t-\Delta t} + \beta_2\epsilon_{t-2\Delta t} + \cdots + \beta_q\epsilon_{t-q\Delta t}) \\ &\quad + \alpha_2 u_{t-2\Delta t}(\beta_2\epsilon_{t-2\Delta t} + \beta_3\epsilon_{t-3\Delta t} + \cdots + \beta_q\epsilon_{t-q\Delta t}) + \cdots \\ &\quad + \alpha_{q-1}u_{t-(q-1)\Delta t}(\beta_{q-1}\epsilon_{t-(q-1)\Delta t} + \beta_q\epsilon_{t-q\Delta t}) + \alpha_q u_{t-q\Delta t}\beta_q\epsilon_{t-q\Delta t}\rangle \\ &= \sum_{i=1}^{q}\sum_{j=i}^{q}\alpha_i\beta_j\varphi_{j-i}\sigma_\epsilon^2.\end{aligned} \tag{A8}$$

A similar approach is taken for the case $p < q$. Then (A7) can be simplified as

$$R_{uu}(k\Delta t) = \begin{cases} \displaystyle\sum_{i=1}^{p}\alpha_i^2 R_{uu}(0) + 2\sum_{i=1}^{p-1}\sum_{j=i+1}^{p}\alpha_i\alpha_j R_{uu}\left((j-i)\Delta t\right) \\ \qquad \displaystyle + \sum_{i=0}^{q}\beta_i^2\sigma_\epsilon^2 + 2\sum_{i=1}^{min\{p,q\}}\sum_{j=i}^{q}\alpha_i\beta_j\varphi_{j-i}\sigma_\epsilon^2, & k = 0, \\ \displaystyle\sum_{i=1}^{p}\alpha_i R_{uu}\left(|k-i|\Delta t\right) + H(q-k)\sum_{i=k}^{q}\beta_i\beta_{i-k}\sigma_\epsilon^2 \\ \qquad \displaystyle + H(q-1-k)\sum_{i=1}^{min\{q-k,p\}}\sum_{j=k+i}^{q}\alpha_i\beta_j\varphi_{j-i-k}\sigma_\epsilon^2, & k \geq 1, \end{cases} \tag{A9}$$

where H is a Heaviside function. Given the parameters α, β and σ_ϵ^2, the linear equations $R_{uu}(0), R_{uu}(\Delta t), \ldots, R_{uu}(p\Delta t)$ can be solved according to (A9) and the autocorrelation can be obtained.

Regardless of the method of calculation used, once the model parameters α, β and σ_ϵ^2 are fitted, the autocorrelation R_{uu} can be obtained explicitly. By comparing the autocorrelation calculated from the model parameters with the autocorrelation of data, it is intuitive to determine the applicability of the ARMA model.

Note that the Heaviside step function in (A9) leads to distinctive ranges of R_{uu}. In particular, when $k \leq \max\{p, q\}$, the behaviour of autocorrelation can only be approximately derived under some assumptions, an example of which is given

in Appendix B. When $k > \max\{p, q\}$, (A9) becomes

$$R_{uu}(k\Delta t) = \sum_{i=1}^{p} \alpha_i R_{uu}\left((k-i)\Delta t\right). \tag{A10}$$

Namely, when the considered data are beyond the model's memory depth ($\max\{p\Delta t, q\Delta t\}$), the autocorrelation is only related to its history. Equation (A10) is a linear homogeneous recurrence relation whose characteristic equation is

$$\lambda^p - \alpha_1\lambda^{p-1} - \alpha_2\lambda^{p-2} - \cdots - \alpha_p = 0. \tag{A11}$$

If (A11) has p unequal roots $\lambda_1, \lambda_2, \ldots, \lambda_p$, its solution has the following form:

$$\lambda = c_1\lambda_1^n + c_2\lambda_2^n + \cdots + c_p\lambda_p^n, \tag{A12}$$

where $c_1, c_2, \ldots, c_p$ are constants. Then R_{uu} has a general expression:

$$R_{uu}(k\Delta t) = \sum_{i=1}^{p} c_i\lambda_i^{k\Delta t} = \sum_{i=1}^{p} c_i \exp\left(k\Delta t \ln\lambda_i\right). \tag{A13}$$

Or if (A11) has t unequal roots $\lambda_1, \lambda_2, \ldots, \lambda_t$, and the multiple numbers of roots are $m_1, m_2, \ldots, m_t$ ($m_i \geq 1$ and $\sum_{i=1}^{t} m_i = p$), then the solution has the following form:

$$\begin{aligned}\lambda = &(c_{1,0}n^0 + c_{1,1}n^1 + \cdots + c_{1,m_1-1}n^{m_1-1})\lambda_1^n + \cdots \\ &+ (c_{t,0}n^0 + c_{t,1}n^1 + \cdots + c_{t,m_t-1}n^{m_t-1})\lambda_t^n,\end{aligned} \tag{A14}$$

where $c_{i,j}(i = 1, \ldots, t,\ j = 0, \ldots, m_i - 1)$ are constants. In this case, R_{uu} is still composed of exponential functions.

The above analysis implies that, beyond the model's memory depth, a set of exponential functions comprise the autocorrelation, which is mainly controlled by the parameters of the AR part and not affected explicitly by the MA part.

A.2. *Power spectral density*

After obtaining the model parameters, we can calculate the power spectral density of the ARMA model:

$$\Phi_{uu}(k_x) = \frac{\sigma_\epsilon^2}{2\pi}\left|\frac{B(\mathrm{i}k_x)}{A(\mathrm{i}k_x)}\right|^2, \tag{A15}$$

where A and B are functions defined in (A2), and k_x is the wavenumber and the corresponding wavelength $\ell = 2\pi/k_x$. Because the power spectra and the autocorrelation are Fourier pairs, they provide the same statistical information of time series with different forms. In addition, the premultiplied power spectra $k_x\Phi_{uu}$ illustrates the contribution of various wavenumber to the total spectra and identifies the wavenumber with the peak spectral density, which is commonly used to reveal large- and very-large-scale motions in boundary-layer turbulence. This work can also indicate how well the model's large-scale exponential behaviour approximates the data by comparing the premultiplied spectra of the ARMA model and the measured ASL data. Details and more information about the ARMA model presented here can be found from Shumway *et al.* (2000).

Appendix B. Logarithmic behaviour of the autocorrelation of the ARMA(1, q) model

Multiplying both sides of the equation of the ARMA(1, q) model (cf. (2.6)) by $u_{t+\tau}$ and taking the average, we get

$$R_{uu}(\tau) = \alpha R_{uu}(\tau + \Delta t) + \sum_{i=0}^{q} \beta_i \langle u_{t+\tau}\epsilon_{t-i\Delta t}\rangle. \tag{B1}$$

The continuous form of (B1) can be expressed as

$$\frac{\mathrm{d}R_{uu}}{\mathrm{d}\tau} = -\tilde{\alpha}R_{uu} + \langle u_{t+\tau}\epsilon_t\rangle + \int_1^q \beta_s \langle u_{t+\tau}\epsilon_{t-s\Delta t}\rangle \,\mathrm{d}s, \tag{B2}$$

where $\beta_0 = 1$ is used and $\tilde{\alpha} = (1-\alpha)/\Delta t$ is a positive constant. Following the same process as calculating (A8), we obtain

$$\begin{aligned}\langle u_{t+\tau}\epsilon_{t-s\Delta t}\rangle &= \left\langle \left(\alpha u_{t+\tau-\Delta t} + \epsilon_{t+\tau} + \sum_{i=1}^{q}\beta_i\epsilon_{t+\tau-i\Delta t}\right)\epsilon_{t-s\Delta t}\right\rangle \\ &= \left\langle \left[\alpha\left(\alpha u_{t+\tau-2\Delta t} + \epsilon_{t+\tau-\Delta t} + \sum_{i=1}^{q}\beta_i\epsilon_{t+\tau-\Delta t-i\Delta t}\right) + \epsilon_{t+\tau}\right.\right. \\ &\quad \left.\left. + \sum_{i=1}^{q}\beta_i\epsilon_{t+\tau-i\Delta t}\right]\epsilon_{t-s\Delta t}\right\rangle = \sigma_\epsilon^2 \sum_{i=0}^{Q}\beta_i\alpha^{Q-i},\end{aligned} \tag{B3}$$

where $Q = \min\{\tau/\Delta t + s, q\}$. Therefore, in a continuous limit,

$$\langle u_{t+\tau}\epsilon_{t-s\Delta t}\rangle = \sigma_\epsilon^2\left(\alpha^{\tau/\Delta t+s} + \int_1^{\tau/\Delta t+s}\beta_{s'}\alpha^{\tau/\Delta t+s-s'}\,\mathrm{d}s'\right). \tag{B4}$$

Assuming β_s' has a power-function form $\beta_s' \sim s'^{-\gamma}$ when $s' > 1$, to the leading order, we obtain

$$\langle u_{t+\tau}\epsilon_{t-s\Delta t}\rangle \sim \int_1^{\tau/\Delta t+s} s'^{-\gamma}\alpha^{\tau/\Delta t+s-s'}\,\mathrm{d}s' \sim (\tau/\Delta t + s)^{-\gamma+1}. \tag{B5}$$

Since $\langle u_{t+\tau}\epsilon_{t-s\Delta t}\rangle$ decreases as s increases according to (B5) and β_s also decays, the integrand in (B2) is the convolution of $\langle u_{t+\tau}\epsilon_t\rangle$ with the kernel function β_s and it is therefore less than $\langle u_{t+\tau}\epsilon_t\rangle$. Thus, the solution of (B2) is dominated by

$$R_{uu} \sim \mathrm{e}^{-\tilde{\alpha}\tau}\left(\int_{\tau_0}^{\tau}\mathrm{e}^{\tilde{\alpha}s'}\langle u_{t+s'}\epsilon_t\rangle\,\mathrm{d}s' + R_{uu}(\tau_0)\right). \tag{B6}$$

Substituting (B5) into the above approximation, we obtain

$$R_{uu} \sim \mathrm{e}^{-\tilde{\alpha}\tau}\int_{\tau_0}^{\tau}\mathrm{e}^{\tilde{\alpha}s'}(s'/\Delta t)^{-\gamma+1}\,\mathrm{d}s'. \tag{B7}$$

Then, taking the leading terms in the Taylor expansion of exponential functions, we get

$$R_{uu} \sim (1 - O(\tilde{\alpha}))\int_{\tau_0}^{\tau}(1 + O(\tilde{\alpha}))\,(s'/\Delta t)^{-\gamma+1}\,\mathrm{d}s' \sim \int_{\tau_0}^{\tau}s'^{-\gamma+1}\,\mathrm{d}s'. \tag{B8}$$

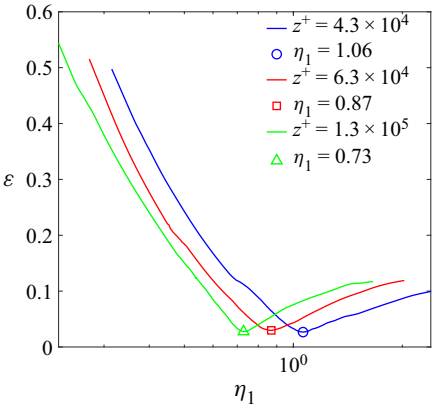

Figure 16. Errors in the optimization of η_1.

z^+	η_1	M_2	ξ_2
4.3×10^4	[1.04, 1.09]	[2.726, 2.729]	[0.723, 0.725]
6.3×10^4	[0.85, 0.89]	[2.803, 2.807]	[0.734, 0.737]
1.3×10^5	[0.72, 0.75]	[2.964, 2.965]	[0.720, 0.722]

Table 1. Uncertainty ranges of M_2, ξ_2 and η_1 in figure 10(a).

Particularly, when $\gamma = 2$, we obtain

$$R_{uu} \sim \ln \tau. \tag{B9}$$

Thus, the logarithmic behaviour of autocorrelation is a consequence of the power law of the MA coefficients β, which justified the fitting result in figure 8(b).

Appendix C. Uncertainty in determining the global expression

As discussed in § 2.3, for a fixed height z with known $\langle u^{+2} \rangle$, the behaviour of the global expression for the second-order structure function is controlled by the transition scale η_1 and small-scale parameters M_2 and ξ_2. To compare the agreement between global expression and ASL data, we define an error

$$\mathcal{E}_0(\eta_1, M_2, \xi_2) = \int_{r_{min}}^{r_{max}} \frac{\left| \langle \Delta u^2 \rangle - G(\eta_1, M_2, \xi_2, r) \right|}{2\langle u^2 \rangle} \, \mathrm{d} \ln \left(\frac{r}{z} \right), \tag{C1}$$

where $G(\eta_1, M_2, \xi_2, r)$ is the global expression of second-order structure function with fixed η_1, M_2 and ξ_2, and r_{min} and r_{max} are the minimum and maximum scales of the structure function, respectively.

Here, we illustrate the uncertainty relating to the choice of η_1 using

$$\mathcal{E}(\eta_1) = \min_{M_2, \xi_2} \mathcal{E}_0(\eta_1, M_2, \xi_2), \tag{C2}$$

which is the minimum error for a fixed η_1. Figure 16 shows the dependence of $\mathcal{E}$ on η_1. These cases correspond to those shown in figure 10(a), where the values of η_1 are determined from the minimum of $\mathcal{E}$. The uncertainty range of η_1 is quantified as the values with $\mathcal{E}$ ranging from $\mathcal{E}_{min}$ to $(1 + 5\,\%)\mathcal{E}_{min}$. Figure 16 and table 1 show a small uncertainty of η_1. The uncertainty ranges of other parameters are summarized in table 1.

References

Anselmet, F., Gagne, Y., Hopfinger, E.J. & Antonia, R.A. 1984 High-order velocity structure functions in turbulent shear flows. *J. Fluid Mech.* **140**, 63–89.

Bailey, S.C.C. & Smits, A.J. 2010 Experimental investigation of the structure of large-and very-large-scale motions in turbulent pipe flow. *J. Fluid Mech.* **651**, 339–356.

Balakumar, B.J. & Adrian, R.J. 2007 Large-and very-large-scale motions in channel and boundary-layer flows. *Phil. Trans. R. Soc.* A **365** (1852), 665–681.

Chamecki, M., Dias, N.L., Salesky, S.T. & Pan, Y. 2017 Scaling laws for the longitudinal structure function in the atmospheric surface layer. *J. Atmos. Sci.* **74** (4), 1127–1147.

Chauhan, K.A. 2007 Study of canonical wall-bounded turbulent flows. PhD thesis, Illinois Institute of Technology.

Choi, B. 2012 *ARMA Model Identification*. Springer Science & Business Media.

Davidson, P.A. & Krogstad, P.-Å. 2009 A simple model for the streamwise fluctuations in the log-law region of a boundary layer. *Phys. Fluids* **21** (5), 055105.

Davidson, P.A. & Krogstad, P.-Å. 2014 A universal scaling for low-order structure functions in the log-law region of smooth-and rough-wall boundary layers. *J. Fluid Mech.* **752**, 140–156.

Davidson, P.A., Krogstad, P.-Å. & Nickels, T.B. 2006*a* A refined interpretation of the logarithmic structure function law in wall layer turbulence. *Phys. Fluids* **18** (6), 065112.

Davidson, P.A., Nickels, T.B. & Krogstad, P.-Å. 2006*b* The logarithmic structure function law in wall-layer turbulence. *J. Fluid Mech.* **550**, 51–60.

Dennis, D.J.C. & Nickels, T.B. 2011 Experimental measurement of large-scale three-dimensional structures in a turbulent boundary layer. Part 1. Vortex packets. *J. Fluid Mech.* **673**, 180–217.

Di Paola, M. 1998 Digital simulation of wind field velocity. *J. Wind Engng Ind. Aerodyn.* **74**, 91–109.

Dilling, S. & MacVicar, B.J. 2017 Cleaning high-frequency velocity profile data with autoregressive moving average (ARMA) models. *Flow Meas. Instrum.* **54**, 68–81.

Ding, M., Nguyen, K.X., Liu, S., Otte, M.J. & Tong, C. 2018 Investigation of the pressure–strain-rate correlation and pressure fluctuations in convective and near neutral atmospheric surface layers. *J. Fluid Mech.* **854**, 88–120.

Faranda, D., Dubrulle, B., Daviaud, F. & Pons, F.M.E. 2014*a* Probing turbulence intermittency via autoregressive moving-average models. *Phys. Rev.* E **90** (6), 061001.

Faranda, D., Pons, F.M.E., Dubrulle, B., Daviaud, F., Saint-Michel, B., Herbert, É. & Cortet, P.-P. 2014*b* Modelling and analysis of turbulent datasets using auto regressive moving average processes. *Phys. Fluids* **26** (10), 105101.

Frisch, U. 1995 *Turbulence: The Legacy of A.N. Kolmogorov*. Cambridge University Press.

Ganapathisubramani, B., Hutchins, N., Hambleton, W.T., Longmire, E.K. & Marusic, I. 2005 Investigation of large-scale coherence in a turbulent boundary layer using two-point correlations. *J. Fluid Mech.* **524**, 57–80.

de Giovanetti, M., Hwang, Y. & Choi, H. 2016 Skin-friction generation by attached eddies in turbulent channel flow. *J. Fluid Mech.* **808**, 511–538.

Guala, M., Hommema, S.E. & Adrian, R.J. 2006 Large-scale and very-large-scale motions in turbulent pipe flow. *J. Fluid Mech.* **554**, 521–542.

Gustenyov, N., Egerer, M., Hultmark, M., Smits, A.J. & Bailey, S.C.C. 2023 Similarity of length scales in high-Reynolds-number wall-bounded flows. *J. Fluid Mech.* **965**, A17.

He, G., Jin, G. & Yang, Y. 2017 Space-time correlations and dynamic coupling in turbulent flows. *Annu. Rev. Fluid Mech.* **49**, 51–70.

Hu, R., Dong, S. & Vinuesa, R. 2023 General attached eddies: scaling laws and cascade self-similarity. *Phys. Rev. Fluids* **8** (4), 044603.

Hutchins, N., Chauhan, K., Marusic, I., Monty, J. & Klewicki, J. 2012 Towards reconciling the large-scale structure of turbulent boundary layers in the atmosphere and laboratory. *Boundary-Layer Meteorol.* **145** (2), 273–306.

Hutchins, N., Hambleton, W.T. & Marusic, I. 2005 Inclined cross-stream stereo particle image velocimetry measurements in turbulent boundary layers. *J. Fluid Mech.* **541**, 21–54.

Hutchins, N. & Marusic, I. 2007 Evidence of very long meandering features in the logarithmic region of turbulent boundary layers. *J. Fluid Mech.* **579**, 1–28.

Hutchins, N., Nickels, T.B., Marusic, I. & Chong, M.S. 2009 Hot-wire spatial resolution issues in wall-bounded turbulence. *J. Fluid Mech.* **635**, 103–136.

Jiménez, J. 2018 Coherent structures in wall-bounded turbulence. *J. Fluid Mech.* **842**, P1.

Kader, B.A. & Yaglom, A.M. 1989 *Spectra and Correlation Functions of Surface Layer Atmospheric Turbulence in Unstable Thermal Stratification*, pp. 387–412. Springer.

KANG, Y., BELUŠIĆ, D. & SMITH-MILES, K. 2014 Detecting and classifying events in noisy time series. *J. Atmos. Sci.* **71** (3), 1090–1104.

KANG, Y., BELUŠIĆ, D. & SMITH-MILES, K. 2015 Classes of structures in the stable atmospheric boundary layer. *Q. J. R. Meteorol. Soc.* **141** (691), 2057–2069.

KAREEM, A. 2008 Numerical simulation of wind effects: a probabilistic perspective. *J. Wind Engng Ind. Aerodyn.* **96** (10–11), 1472–1497.

KIM, K.C. & ADRIAN, R.J. 1999 Very large-scale motion in the outer layer. *Phys. Fluids* **11** (2), 417–422.

KLEINHANS, D., FRIEDRICH, R., SCHAFFARCZYK, A.P. & PEINKE, J. 2009 Synthetic turbulence models for wind turbine applications. In *Progress in Turbulence III* (ed. J. Peinke, M. Oberlack & A. Talamelli), pp. 111–114. Springer.

KOLMOGOROV, A.N. 1941 The local structure of turbulence in incompressible viscous fluid for very large Reynolds numbers. *C. R. Acad. Sci. URSS* **30**, 301–305.

KOVASZNAY, L.S.G., KIBENS, V. & BLACKWELDER, R.F. 1970 Large-scale motion in the intermittent region of a turbulent boundary layer. *J. Fluid Mech.* **41** (2), 283–325.

KRENK, S. & MØLLER, R.N. 2019 Turbulent wind field representation and conditional mean-field simulation. *Proc. R. Soc.* A **475** (2223), 20180887.

KUSIAK, A., ZHENG, H. & SONG, Z. 2009 Short-term prediction of wind farm power: a data mining approach. *IEEE Trans. Energy Convers.* **24** (1), 125–136.

LEE, M. & MOSER, R.D. 2015 Direct numerical simulation of turbulent channel flow up to $Re_\tau \approx 5200$. *J. Fluid Mech.* **774**, 395–415.

LEE, J.H. & SUNG, H.J. 2011 Very-large-scale motions in a turbulent boundary layer. *J. Fluid Mech.* **673**, 80–120.

LI, X., HUTCHINS, N., ZHENG, X., MARUSIC, I. & BAARS, W.J. 2022 Scale-dependent inclination angle of turbulent structures in stratified atmospheric surface layers. *J. Fluid Mech.* **942**, A38.

LIU, H., ERDEM, E. & SHI, J. 2011 Comprehensive evaluation of ARMA–GARCH (-M) approaches for modeling the mean and volatility of wind speed. *Appl. Energy* **88** (3), 724–732.

LIU, H., HE, X. & ZHENG, X. 2021 An investigation of particles effects on wall-normal velocity fluctuations in sand-laden atmospheric surface layer flows. *Phys. Fluids* **33** (10), 103309.

LIU, H., WANG, G. & ZHENG, X. 2017 Spatial length scales of large-scale structures in atmospheric surface layers. *Phys. Rev. Fluids* **2**, 064606.

LIU, H., WANG, G. & ZHENG, X. 2019*a* Amplitude modulation between multi-scale turbulent motions in high-Reynolds-number atmospheric surface layers. *J. Fluid Mech.* **861**, 585–607.

LIU, H., WANG, G. & ZHENG, X. 2019*b* Three-dimensional representation of large-scale structures based on observations in atmospheric surface layers. *J. Geophys. Res.* **124** (20), 10753–10771.

MARUSIC, I. & KUNKEL, G.J. 2003 Streamwise turbulence intensity formulation for flat-plate boundary layers. *Phys. Fluids* **15** (8), 2461–2464.

MARUSIC, I. & MONTY, J.P. 2019 Attached eddy model of wall turbulence. *Annu. Rev. Fluid Mech.* **51**, 49–74.

MARUSIC, I., MONTY, J.P., HULTMARK, M. & SMITS, A.J. 2013 On the logarithmic region in wall turbulence. *J. Fluid Mech.* **716**, R3.

MENEVEAU, C. & MARUSIC, I. 2013 Generalized logarithmic law for high-order moments in turbulent boundary layers. *J. Fluid Mech.* **719**, R1.

MENEVEAU, C. & SREENIVASAN, K.R. 1987 Simple multifractal cascade model for fully developed turbulence. *Phys. Rev. Lett.* **59** (13), 1424.

MONIN, A.S. & OBUKHOV, A.M. 1954 Basic laws of turbulent mixing in the atmosphere near the ground. *Tr. Geofiz. Inst. Akad. Nauk SSSR* **24** (151), 163–187.

MONKEWITZ, P.A. 2022 Asymptotics of streamwise Reynolds stress in wall turbulence. *J. Fluid Mech.* **931**, A18.

OBUKHOV, A. 1946 Turbulence in thermally inhomogeneous atmosphere. *Tr. Inst. Teor. Geofiz. Akad. Nauk SSSR* **1**, 95–115.

ÖNDER, A. & MEYERS, J. 2018 On the interaction of very-large-scale motions in a neutral atmospheric boundary layer with a row of wind turbines. *J. Fluid Mech.* **841**, 1040–1072.

O'NEILL, P.L., NICOLAIDES, D., HONNERY, D., SORIA, J. 2004 Autocorrelation functions and the determination of integral length with reference to experimental and numerical data. In *15th Australasian Fluid Mechanics Conference* (ed. M. Behnia, W. Lin & G.D. McBain), vol. 1, pp. 1–4. University of Sydney.

PAN, Y. & CHAMECKI, M. 2016 A scaling law for the shear-production range of second-order structure functions. *J. Fluid Mech.* **801**, 459–474.

POPE, S.B. 2000 *Turbulent Flows*. Cambridge University Press.

PUCCIONI, M., CALAF, M., PARDYJAK, E.R., HOCH, S., MORRISON, T.J., PERELET, A. & IUNGO, G.V. 2023 Identification of the energy contributions associated with wall-attached eddies and very-large-scale motions in the near-neutral atmospheric surface layer through wind LiDAR measurements. *J. Fluid Mech.* **955**, A39.

RAZAZ, M. & KAWANISI, K. 2011 Signal post-processing for acoustic velocimeters: detecting and replacing spikes. *Meas. Sci. Technol.* **22** (12), 125404.

ROBINSON, S.K. 1991 Coherent motions in the turbulent boundary layer. *Annu. Rev. Fluid Mech.* **23** (1), 601–639.

ROSSI, R., LAZZARI, M. & VITALIANI, R. 2004 Wind field simulation for structural engineering purposes. *Intl J. Numer. Meth. Engng* **61** (5), 738–763.

SAMIEE, M., AKHAVAN-SAFAEI, A. & ZAYERNOURI, M. 2022 Tempered fractional LES modeling. *J. Fluid Mech.* **932**, A4.

SCHMIDT, O.T., TOWNE, A., RIGAS, G., COLONIUS, T. & BRÈS, G.A. 2018 Spectral analysis of jet turbulence. *J. Fluid Mech.* **855**, 953–982.

SCHMITT, F.G. & HUANG, Y. 2016 *Stochastic Analysis of Scaling Time Series: From Turbulence Theory to Applications*. Cambridge University Press.

SCHOPPA, W. & HUSSAIN, F. 2002 Coherent structure generation in near-wall turbulence. *J. Fluid Mech.* **453**, 57–108.

SFETSOS, A. 2002 A novel approach for the forecasting of mean hourly wind speed time series. *Renew. Energy* **27** (2), 163–174.

SHE, Z.S. & LEVEQUE, E. 1994 Universal scaling laws in fully developed turbulence. *Phys. Rev. Lett.* **72** (3), 336.

SHUMWAY, R.H., STOFFER, D.S. & STOFFER, D.S. 2000 *Time Series Analysis and Its Applications*, vol. 3. Springer.

SILLERO, J.A., JIMÉNEZ, J. & MOSER, R.D. 2014 Two-point statistics for turbulent boundary layers and channels at Reynolds numbers up to $\delta^+ \approx 2000$. *Phys. Fluids* **26** (10), 105109.

DE SILVA, C.M., HUTCHINS, N. & MARUSIC, I. 2016 Uniform momentum zones in turbulent boundary layers. *J. Fluid Mech.* **786**, 309–331.

DE SILVA, C.M., MARUSIC, I., WOODCOCK, J.D. & MENEVEAU, C. 2015 Scaling of second-and higher-order structure functions in turbulent boundary layers. *J. Fluid Mech.* **769**, 654–686.

TAYLOR, G.I. 1921 Diffusion by continuous movements. *Proc. Lond. Math. Soc.* **2** (1), 196–212.

TAYLOR, G.I. 1938 The spectrum of turbulence. *Proc. R. Soc. Lond.* **164** (919), 476–490.

TENNEKES, H. 1979 The exponential Lagrangian correlation function and turbulent diffusion in the inertial subrange. *Atmos. Environ.* **13** (11), 1565–1567.

TENNEKES, H. 1982 *Similarity Relations, Scaling Laws and Spectral Dynamics*, pp. 37–68. Springer.

THOMSON, D.J. 1987 Criteria for the selection of stochastic models of particle trajectories in turbulent flows. *J. Fluid Mech.* **180**, 529–556.

TONG, C. & DING, M. 2019 Multi-point Monin–Obukhov similarity in the convective atmospheric surface layer using matched asymptotic expansions. *J. Fluid Mech.* **864**, 640–669.

TONG, C. & NGUYEN, K.X. 2015 Multipoint Monin–Obukhov similarity and its application to turbulence spectra in the convective atmospheric surface layer. *J. Atmos. Sci.* **72** (11), 4337–4348.

TOWNSEND, A.A. 1961 Equilibrium layers and wall turbulence. *J. Fluid Mech.* **11** (1), 97–120.

TOWNSEND, A.A.R. 1976 *The Structure of Turbulent Shear Flow*. Cambridge University Press.

TRITTON, D.J. 2012 *Physical Fluid Dynamics*. Springer Science & Business Media.

TUTKUN, M., GEORGE, W.K., DELVILLE, J., STANISLAS, M., JOHANSSON, P., FOUCAUT, J.-M. & COUDERT, S. 2009 Two-point correlations in high Reynolds number flat plate turbulent boundary layers. *J. Turbul.* **10**, N21.

VERCAUTEREN, N., BOYKO, V., FARANDA, D. & STIPERSKI, I. 2019 Scale interactions and anisotropy in stable boundary layers. *Q. J. R. Meteorol. Soc.* **145** (722), 1799–1813.

VERCAUTEREN, N. & KLEIN, R. 2015 A clustering method to characterize intermittent bursts of turbulence and interaction with submesomotions in the stable boundary layer. *J. Atmos. Sci.* **72** (4), 1504–1517.

VERCAUTEREN, N., MAHRT, L. & KLEIN, R. 2016 Investigation of interactions between scales of motion in the stable boundary layer. *Q. J. R. Meteorol. Soc.* **142** (699), 2424–2433.

VOLINO, R.J., SCHULTZ, M.P. & FLACK, K.A. 2007 Turbulence structure in rough-and smooth-wall boundary layers. *J. Fluid Mech.* **592**, 263–293.

WALLACE, J.M. 2014 Space-time correlations in turbulent flow: a review. *Theor. Appl. Mech. Lett.* **4** (2), 022003.

WANG, G., GU, H. & ZHENG, X. 2020 Large scale structures of turbulent flows in the atmospheric surface layer with and without sand. *Phys. Fluids* **32** (10), 106604.

WANG, G. & ZHENG, X. 2016 Very large scale motions in the atmospheric surface layer: a field investigation. *J. Fluid Mech.* **802**, 464–489.

WYNGAARD, J.C. & COTÉ, O.R. 1971 The budgets of turbulent kinetic energy and temperature variance in the atmospheric surface layer. *J. Atmos. Sci.* **28** (2), 190–201.

WYNGAARD, J.C., COTÉ, O.R. & IZUMI, Y. 1971 Local free convection, similarity, and the budgets of shear stress and heat flux. *J. Atmos. Sci.* **28** (7), 1171–1182.

XIE, J.-H., DE SILVA, C., BAIDYA, R., YANG, X.I.A. & HU, R. 2021 Third-order structure function in the logarithmic layer of boundary-layer turbulence. *Phys. Rev. Fluids* **6** (7), 074602.

YAGLOM, A.M. 1994 Fluctuation spectra and variances in convective turbulent boundary layers: a reevaluation of old models. *Phys. Fluids* **6** (2), 962–972.

YANG, X.I.A., BAIDYA, R., JOHNSON, P., MARUSIC, I. & MENEVEAU, C. 2017 Structure function tensor scaling in the logarithmic region derived from the attached eddy model of wall-bounded turbulent flows. *Phys. Rev. Fluids* **2** (6), 064602.

YANG, Q., WILLIS, A.P. & HWANG, Y. 2019 Exact coherent states of attached eddies in channel flow. *J. Fluid Mech.* **862**, 1029–1059.

ZHANG, F.-C., XIE, J.-H., CHEN, S.X. & ZHENG, X. 2023 Analysing and predicting streamwise velocity fluctuations in nonstationary atmospheric surface layers using the ARMA-GARCH model. In *IUTAM Symposium on Turbulent Structure and Particles-Turbulence Interaction* (ed. X. Zheng & S. Balachandar), pp. 104–116. Springer.

ZHANG, F.-C., XIE, J.-H. & ZHENG, X. 2022 Structure-function based study on the logarithmic region in atmospheric surface layer with and without sand. *Phys. Rev. Fluids* **7** (8), 084609.

ZHOU, J., ADRIAN, R.J., BALACHANDAR, S. & KENDALL, T.M. 1999 Mechanisms for generating coherent packets of hairpin vortices in channel flow. *J. Fluid Mech.* **387**, 353–396.